DIPLOMARBEIT

Titel der Diplomarbeit

„Laser Beam Engineering for Material Processing“

Verfasser

Dipl. Ing. (FH) Christian Haselberger

angestrebter akademischer Grad

Magister der Naturwissenschaften (Mag. rer. nat.)

Wien, 2009

Studienkennzahl lt. Studienblatt:	A 419
Studienrichtung lt. Studienblatt:	Chemie
Betreuerin / Betreuer:	Univ.-Prof. Dipl.-Ing. Dr. Wolfgang Kautek

Contents

Abstract

A main focus of this diploma work was the characterization of femtosecond laser pulses. A LabVIEW program for autocorrelation measurements was adapted to deliver results at an interval of up to 2 Hz and a FROG (frequency-resolved optical gating) device was developed to characterize the phase of laser pulses. Ablation experiments were carried out to determine the dependence of the fs-laser ablation threshold on the thickness of thin diamond like films. These experiments served as preparation for the setup, adjustment, and calibration of a pulse shaper in a new configuration with a high-power femtosecond oscillator.

Kurzfassung

Ein wichtiger Bestandteil dieser Diplomarbeit war die Charakterisierung von Femtosekunden-Laserpulsen. Dazu wurde das bestehende LabVIEW Programm für die Autokorrelationsmessungen adaptiert und ermöglicht nun Messungen mit einer Geschwindigkeit von bis zu 2 Hz. Ebenfalls wurde ein FROG (frequency-resolved optical gating) aufgebaut, womit auch die Phasenanteile der Femtosekunden-Laserpulse gemessen werden können. Mittels Ablationsexperimenten wurde die Abhängigkeit der Ablationsschwelle von der Filmdicke von diamantähnlichen Kohlenstoffschichten ermittelt. Zur erweiterten Durchführung von Ablationsexperimenten wurden der Aufbau, die Justage und die Kalibrierung eines Pulsformers in Kopplung eines leistungsstarken Femtosekundenoszillators realisiert.

1 Introduction

Lasers (light amplification by stimulated emission of radiation) and their technology are known since 50 years [1]. There are many different fields of application like cutting, welding, and labelling in industrial material processing and in diagnostics and surgery in medical science. Lasers normally are known from television or laser shows because of their strong and impressive colour. Of course the colours are impressive as it can be seen inside the laser oscillator used in our lab (see Figure 1) but this is only a side effect.

There is much attention on pulsed lasers with pulse lengths in the femtosecond and recently in the attosecond regime. Thermal diffusion control in femtosecond laser processing of solids is restricted to nanoscale dimensions, which has been one of the reasons of the breakthrough of this category of lasers in materials machining [2]. That means that femtosecond excitation provides the promising perspective that laser radiation interaction with the evolving plasma is minimized and that heat affected zones are reduced into the nanoscale range in contrast to pico- and nanosecond laser processing. Near-infrared ultrashort laser pulses down to durations of 5 fs yielded unexpected machining qualities characterised by high precision and deterministic features [3].

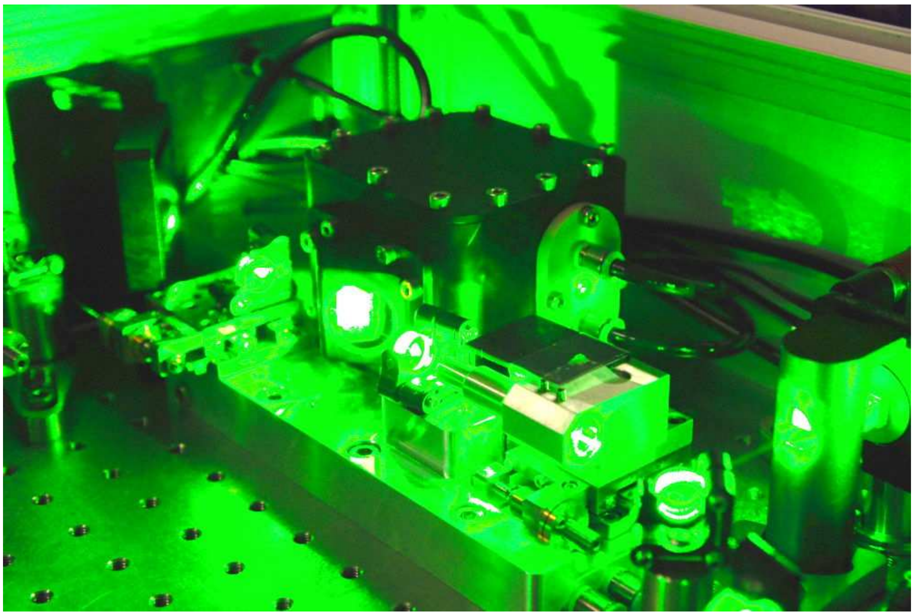

Figure 1: Impressive green scattered light inside the sub-60-fs high-power 11 MHz laser system with fs-power-oscillator technology used in our lab

A laser-technological objective was also the adaptive laser beam engineering for material processing. This new technological approach explores the excitation of optical phonons in order to reduce processing energy thresholds. Theory suggests a resonant coherent enhancement of the phonon modes excited by femtosecond laser pulses in dielectric media which and can be measured with a transient transmission setup [4]. There is experimental work proving this for LiTaO3 [5]. Coherent phonons have been shown to exist in technologically relevant materials like α-quartz [6]. This opens the potential for nanostructuring of optical materials by adaptive irradiation systems on the basis of a novel industrial-suited 60 fs-laser oscillator technology integrated with a pulse shaper allowing temporal design of 60 fs laser pulses. The temporal pulse shaping generated by phase modulation will be followed by adaptive, feedback-controlled material processing. Thus, a cost-efficient nanostructuring technology of photonic materials comes within sight.

In the following work a pulsed Ti:sapphire laser with a pulse length of 60 fs was used in combinations with an intensity autocorrelator, a FROG, a pulse shaper and a microscope to carry out fs-laser ablation of thin diamond like carbon films. Therefore chapter 2 will give an overview of the theoretical background of all methods and devices used during the work. In chapter 3 the whole setup including the measurement devices will be introduced and chapter 4 contains results and discussion. The conclusion and outlook will be in chapter 5. In the appendix the LabVIEW program written for acquiring the autocorrelation trace will be described.

2 Theoretical Background

This chapter describes the background of all used experimental techniques. It is described how laser pulses are generated and how their spectral and temporal properties can be influenced and measured.

2.1 The Basics

What is an ultrashort laser pulse? There is a simple answer: it is a very short burst of electro-magnetic energy. Mathematically the pulse electric field *E(x,y,z,t)* is described by the product of a sine wave and a pulse-envelope function. The electric field is dependent on space and time. For simplicity some assumptions are made. The vector character of the pulse electric field is ignored because the field is treated as linearly polarized. Although we are mainly interested in the temporal features of the pulse and therefore ignore the spatial part of the field. The resulting time-dependent electric field *E(t)* can be written as [7]

$$E(t) = \frac{1}{2}\sqrt{I(t)} \cdot e^{i(\omega_0 t - \phi(t))} + c.c. \tag{1}$$

Where ω_0 is the carrier angular frequency and *I(t)* and $\phi(t)$ are the time-dependent intensity and phase of the pulse. The term *c.c.* means complex conjugate and is required to get a real pulse field. For simpler mathematics the complex-conjugate term is ignored which is commonly called the “analytic signal” approximation and this yields a complex electric pulse field which is used for further mathematical descriptions:

$$E(t) = \sqrt{I(t)} \cdot e^{-i\phi(t)} \tag{2}$$

The carrier wave $e^{i\omega_0 t}$ is removed because it cannot be measured reliably and makes mathematics easier too. As the complex-conjugate term is removed the real part is taken twice. The yielded equation can be solved for the intensity which can be measured for example by the intensity autocorrelation described in chapter 2.3.2

$$I(t) = \left|E(t)\right|^2 \tag{3}$$

The phase can be measured by FROG described in chapter 2.3.3

$$\phi(t) = -\arctan\frac{\mathrm{Im}(E(t))}{\mathrm{Re}(E(t))} \tag{4}$$

A sample pulse is shown in Figure 2 where the different meanings of the electro-magnetic field, the amplitude of field, and the intensity are shown. An important property of the pulse is the pulse length which is normally defined as the full width at half maximum (FWHM).

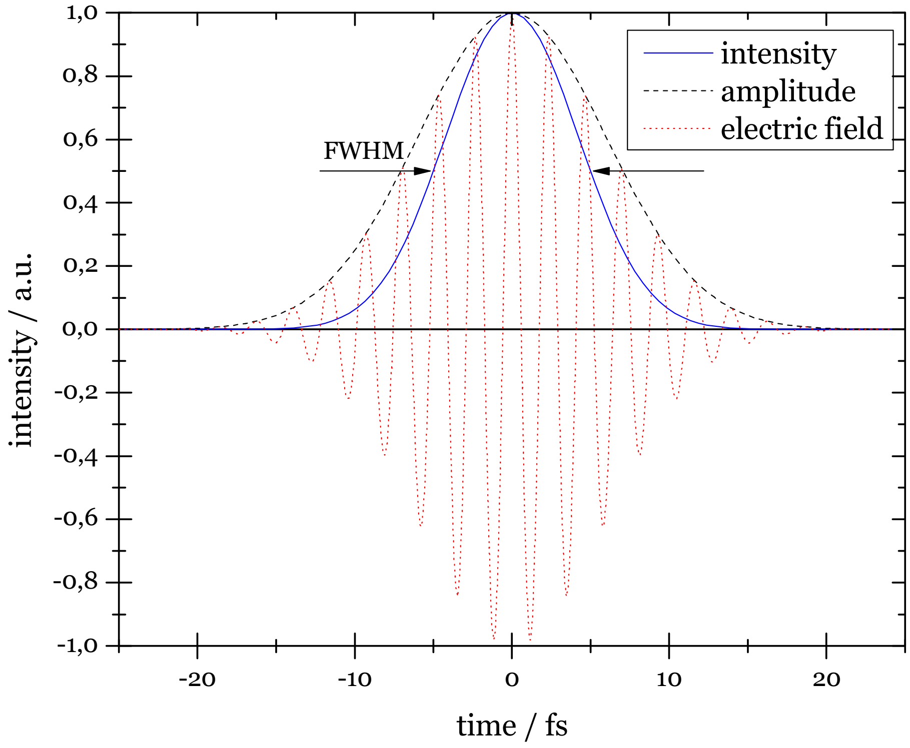

Figure 2: A Gaussian laser pulse showing the amplitude and the electric field and the corresponding intensity

The pulse electric field can also be described in the frequency domain. The Fourier transform of the time domain field yields the frequency domain field

$$\tilde{E}(\omega) = \int_{-\infty}^{\infty} E(t) e^{-i\omega t} dt \tag{5}$$

and in terms of intensity *$S(\omega)$* and phase *$\varphi(\omega)$*

$$\tilde{E}(\omega) = \sqrt{S(\omega)} \cdot e^{-i\varphi(\omega)} \tag{6}$$

$S(\omega)$ is the frequency spectrum which will be measured with a spectrometer and the spectral phase can be retrieved from the FROG trace. The inverse Fourier transform of the frequency domain yields the time domain electric field

$$E(t) = \frac{1}{2\pi} \int_{-\infty}^{\infty} \tilde{E}(t) e^{i\omega t} d\omega \tag{7}$$

In the laboratory the time dependent intensity is the most interesting part but as there is a relation to the frequency domain this is being checked too. A deviation in spectral phase changes the pulse shape in time domain.

The time and frequency dependent phases can be written as a Taylor series expansion

$$\phi(t) = \phi_0 + t\phi_1 + \frac{t^2\phi_2}{2} + \ldots \tag{8}$$

$$\varphi(\omega) = \varphi_0 + (\omega - \omega_0)\varphi_1 + \frac{(\omega - \omega_0)^2\varphi_2}{2} + \ldots \tag{9}$$

The first order term $t\phi_1$ corresponds to a shift in time and describes the time delay of the pulse relative to the pulse without delay. The greater this term is the later or earlier the pulse arrives. The second order term is called linear chirp and describes the linear dependence of the velocity vs. frequency of light. One example of linear dispersion is glass where red light travels faster than blue light. For optical elements the group delay dispersion is introduced which describes the different velocities of light in medium dependent on the frequency. For an optical element this describes the broadening of a laser pulse while passing it.

A further definition is the time-bandwidth product $\Delta t \Delta \nu$ which gives a correlation between pulse length and spectral width. Consequently a large spectral width yields a short pulse duration. It can be shown that for any spectrum the shortest pulse in time always occurs for a constant spectral phase $\varphi(\omega)$. These pulses are called Fourier limited pulses.

2.2 Pulse Generation

So far a mathematical description of the laser pulses was made. The generation of them with physical components will be described next.

2.2.1 Principle

The laser which generates the optical pulses usually consists of an optical resonator (Figure 3) build by two mirrors and a gain medium. The very beginning of the light is spontaneous emission (fluorescence) of the gain medium. This light can travel between the two mirrors and is amplified through the gain medium (a laser crystal) each round trip due to stimulated emission. This process is described in more details in [8, 9].

Without a gain medium the circulating light would become weaker in each resonator round trip because of the losses of the optical components, e.g. mirrors have a reflection less than 100%. The gain medium has to amplify the light more than the losses weaken it to get an overall amplification. Therefore it needs an external energy supply to get “pumped”, e.g. in form of a pump light or an electric current. At the output coupler mirror a fraction of the light circulating in the resonator is transmitted resulting in the laser beam useable for the experiments. The output laser light can be continuous or pulsed depending on the resonator design and the gain medium. For continuous operation only a single resonator mode (=a wave with only one fixed frequency) can oscillate. For mode-locked lasers, the bandwidth (=width of the frequency spectrum) can be very large, which means multiple modes oscillate in the resonator and result under some circumstances in laser pulses [10].

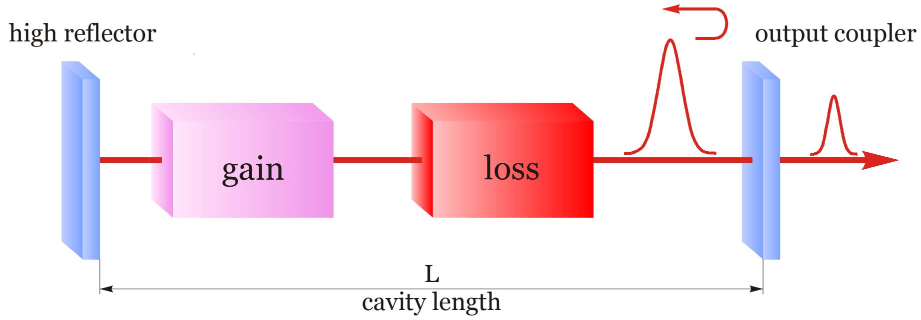

Figure 3: A laser resonator and its components

A single mode is a single wave and has to fulfil the self-consistency condition which means it has to reproduce its exact transverse amplitude profile (without any rescaling) only after a full resonator round trip. The phase must also be reproduced after one round trip and so has to be an integer multiple of 2π. The phase condition limits the resonator modes to certain optical frequencies [10]. When superposing these modes with a fixed phase pulses are obtained which is called “mode locking”. There are two methods namely active mode locking (needs an additional electronic circuit) which is usually limited to picosecond pulses and passive mode locking which allows much shorter pulses, e.g. femtosecond pulses [11].

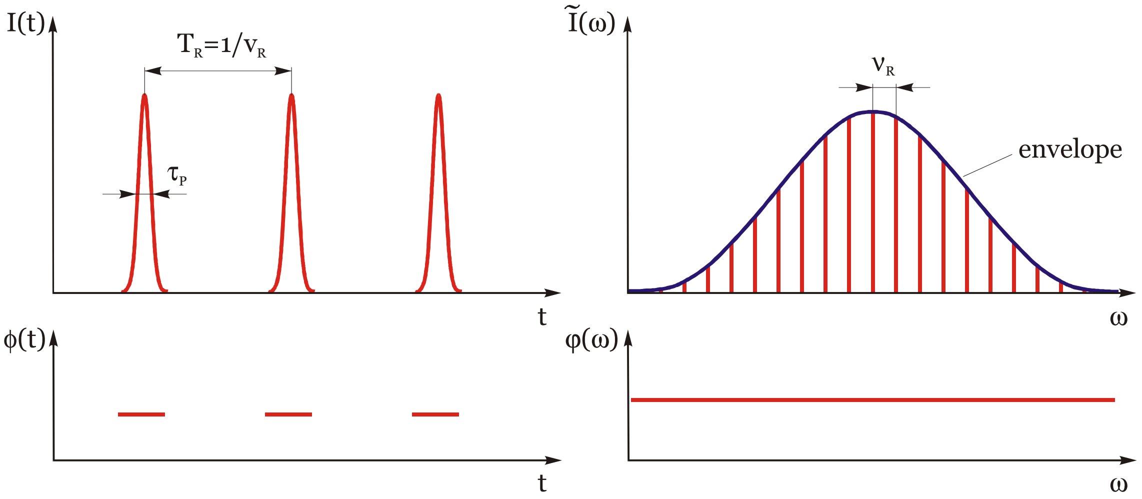

Figure 4: A pulse train (left) and the frequency spectrum (right) of a mode locked laser

Mode locking produces a pulse train with constant temporal distances in the time domain where the distance depends on the round-trip time T_R of a pulse inside the laser cavity (see Figure 4). In the frequency domain a frequency comb with constant spacing which equals the repetition rate ν_R is observed. If the resolution of the spectrometer is not high enough the envelope of the frequency comb will be measured. The round-trip time and the repetition rate are indirect proportional and depend on the length of the laser resonator. The longer the resonator the lower is the repetition rate. The pulse length τ_P and the spectral width $\Delta\nu_P$ are inversely proportional [11]. The shortest pulses (Fourier limited) can be obtained with a flat phase in time and frequency domain as shown in Figure 4. Depending on the gain medium laser light (continuous wave or pulsed) at different centre wavelengths and energies can be produced. One example for the gain medium is the Ti:sapphire crystal.

2.2.2 Ti:Sapphire Oscillator

The titanium sapphire crystal (Al_2O_3 crystal doped with titanium ions) is most widely used for solid state lasers. It can operate over a wide wavelength range 660-1180nm [12]. Commercially available Ti:sapphire lasers are typically pumped with a frequency doubled Nd:YAG or Nd:YO_4 laser at 532 nm. Pulse lengths less than 5 fs have already been generated using Ti:sapphire. One oscillation of the electric field, which lasts 2.7 fs at 800 nm for Ti:sapphire, is the theoretical limit for the pulse length [13].

It is a goal to maximize the energy of a single pulse but because of the short duration the peak intensity is very high which leads to a physical boundary of the crystal. One solution is the elongation of the resonator length because the pulse energy is directly proportional to the laser cavity length [14]. A second possibility is to positively or negatively disperse (=stretch) the pulse to get smaller peak intensities inside the resonator. But then the pulses have to be compressed outside the resonator to get short pulses again [15]. A possible oscillator setup is shown in Figure 18 in the experimental section.

2.2.3 Prism Compression

There are different approaches to compensate the positive dispersion of optical pulses. One is the use of diffraction gratings to generate negative dispersion, but this introduces relatively large losses and is not easy to adjust to zero dispersion [16]. Another approach is the use of prism pairs which provide low loss and they are easy to adjust from negative to positive dispersion values [17]. The principle arrangement is shown in Figure 5 consisting of four identical prisms. The p-polarized beam enters at the Brewster's angle at each surface for minimum reflection losses. In this configuration negative dispersion can be obtained because different wavelength components will travel on slightly different optical paths, e.g. the phase delay for the blue component is larger than that for the red component. The negative dispersion obtained from this effect is proportional to the prism separation *d*. But there is also positive dispersion resulting from propagation in the prism which can be easily adjusted by changing how much of the prism II is inserted into the optical path [11]. An arrangement with a negative introduced dispersion with only two prisms can be obtained by placing a mirror at the symmetry plane of the four prism arrangement marked in Figure 5. Consequently the incident and return beam are collinear and in opposite directions. Beam separation can be achieved by an offset of the return beam in a different height.

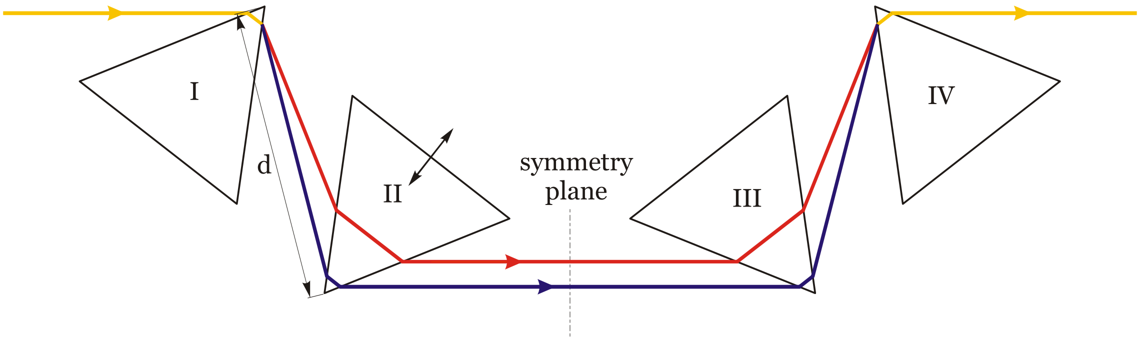

Figure 5: A four-prism compressor introducing negative dispersion

2.2.4 Pockels Cell

The oscillator of a pulsed laser system generates a train of pulses with a constant repetition rate, i.e. the time between two consecutive pulses is constant depending on the length of the resonator. For various reasons it is often necessary to pick certain pulses from such a train, transmit them, and block all others. This can be realized by a pulse picker, which consists of two crossed polarizers and a Pockels cell in between [10]. In this configuration no light can pass. But applying a certain high voltage (=half-wave voltage [10]) to the Pockels cell, it acts like a λ/2-plate and turns the plane of polarization of the incident light 90° and allows the light to pass through the arrangement. Continuous modulation of the high voltage allows the reduction of the repetition rate as well as the transmission of a single pulse.

2.3 Pulse Characterization

On the previous pages the generation and manipulation of laser pulses and pulse train was described. But before such pulses are used for experiments, it is necessary to characterize these pulses properly to provide information about the experimental conditions.

Optical pulses can be characterized with many different parameters:

- temporal and spectral intensity
- temporal and spectral phase
- temporal pulse duration
- pulse energy
- peak power
- repetition rate
- beam shape and diameter

There are methods of complete pulse characterization [18] to receive the electric field dependent on time, and the intensity and phase of the spectrum of ultrashort laser pulses. The two most widely used techniques are FROG (frequency-resolved optical gating) [7] which will be described in chapter 2.3.3 and SPIDER (spectral interferometry for direct electric-field reconstruction) [19]. Both measure the time- and frequency-dependent intensity and phase of a laser pulse indirectly because up to now there is no electronic device which is fast enough to measure these properties directly.

2.3.1 Energy and Power

Measurement of the energy of a laser pulse is usually done using a pyroelectric device. The increase of the temperature due the energy of the laser pulse gives a proportional electrical response. According to the thermal load the material needs time to return to the original value before a new measurement can be started. This fact limits the maximum measurable repetition rate.

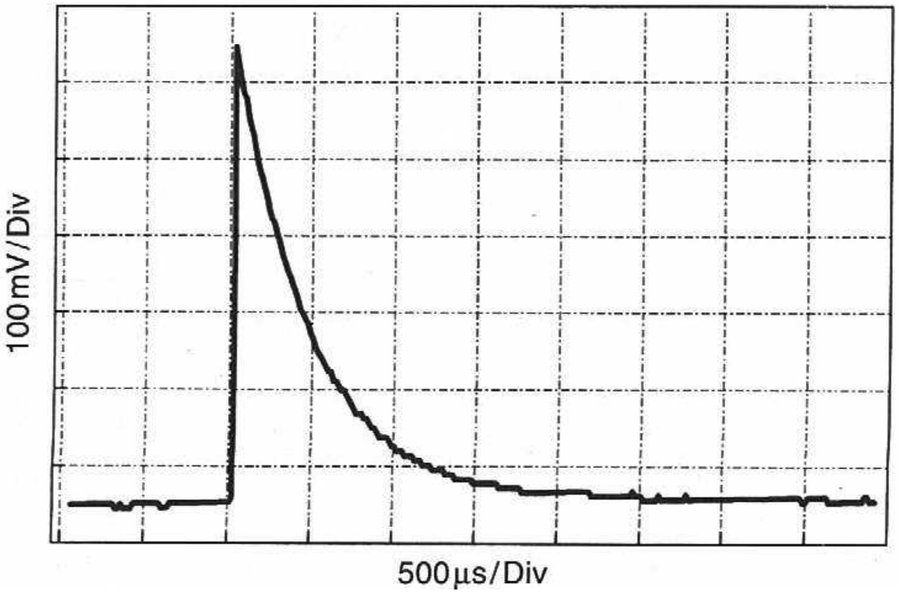

Figure 6: Typical electrical response of a pyroelectric detector [9]

The electrical response of pyroelectric devices is constant over a wide wavelength range and therefore can be used for many different wavelengths without recalibration. In Figure 6 there is a typical response versus time of such a detector where the peak value of the signal is proportional to the pulse energy [9].

For high repetition rates the measurement of the average power is the only way to get the pulse energy. Therefore the knowledge of the repetition rate is required to calculate the energy from the power. The use of a thermoelectric photodetector with a long thermal time constant leads us to an equilibrium temperature depending on the average power. Dividing the average power by the repetition rate yields the pulse energy.

2.3.2 Intensity Autocorrelation

The characterization of the temporal profile of the laser pulse is the basis of any laser optimization. Generally a short event is measured with an even shorter event. But on the femtosecond time scale this is hardly possible and there is no electric device to measure the pulse directly. So an approach is introduced to measure the pulse by itself. This technique is called autocorrelation [7].

The intensity autocorrelation (in this work also referred to as autocorrelation), $A^{(2)}(\tau)$, is one possible implementation of this technique and yields the temporal intensity vs. time of a laser pulse. The setup is shown in Figure 7. The pulse to be analyzed is split into two where one is variably delayed with respect to the other. Both parts are then focused, spatially overlapping, onto a nonlinear optical medium, such as a second-harmonic-generation (SHG) crystal. There is also a collinear setup which can be found in [9].

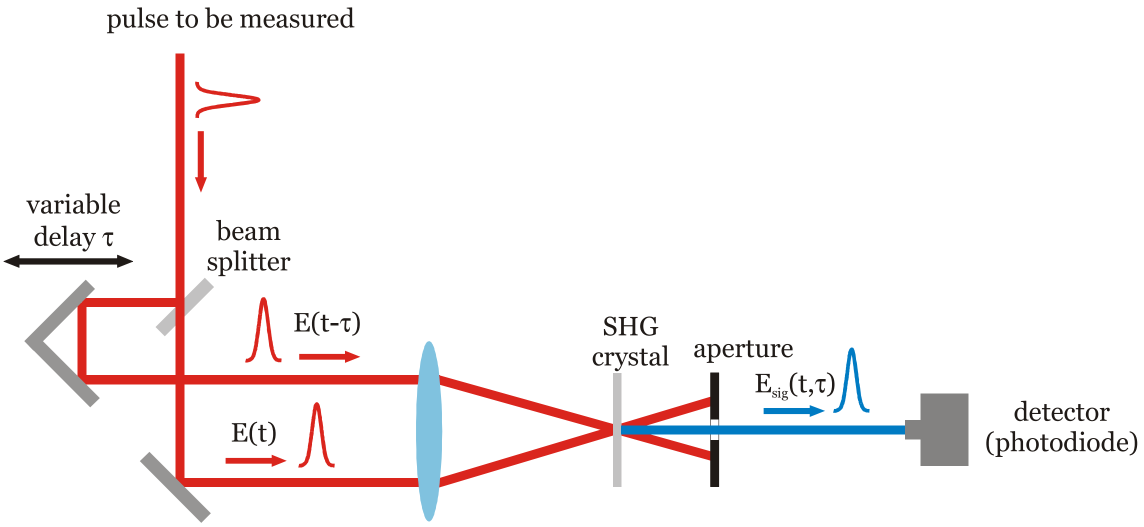

Figure 7: Setup for an intensity autocorrelator using second-harmonic generation

The crystal produces light with double frequency (half wavelength) of the incident light, e.g. 400 nm in the case of a 800 nm Ti:sapphire laser which has an electric field proportional to the two input pulses [7]

$$E_{sig}^{SHG}(t,\tau) \propto E(t)E(t-\tau) \tag{10}$$

and same for the intensity

$$I_{sig}^{SHG}(t,\tau) \propto I(t)I(t-\tau) \tag{11}$$

Because the detectors are too slow to resolve $I_{sig}^{SHG}(t,\tau)$ the integral over time will be measured

$$A^{(2)}(\tau) = \int_{-\infty}^{\infty} I(t)I(t-\tau)dt \tag{12}$$

The intensity $A^{(2)}(\tau)$ depends on the delay τ and there will not be an intensity if the delay is too large and the pulses are not overlapping any more. The intensity is recorded with a detector (commonly a photodiode) and the FWHM (full width at half maximum) of the autocorrelation can be obtained. To get the FWHM of the laser pulse a factor has to be considered which depends on the pulse shape.

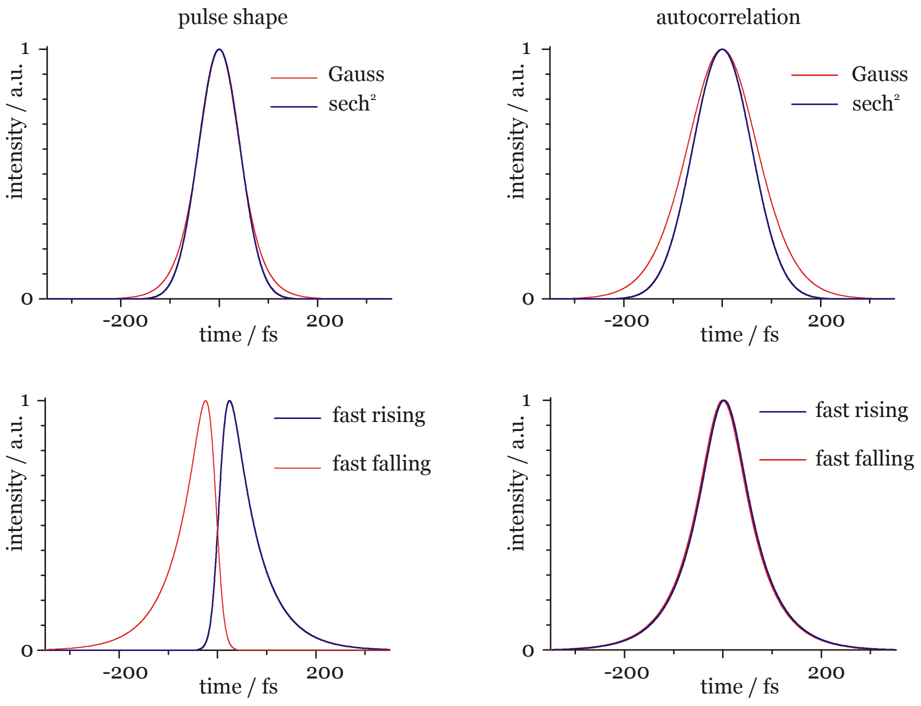
pulse shape

autocorrelation

Figure 8: Different pulse shapes (left) and their corresponding autocorrelation trace (right) (modified [14])

In the top row of Figure 8 a Gaussian and a sech² pulse with 100 fs is shown and the corresponding autocorrelation. As shown the autocorrelation function for the Gaussian pulse is broader than for the sech² pulse. So the knowledge of the pulse shape is essential for correct determination of the pulse length. If the pulse shape is Gaussian then the FWHM of the autocorrelation has to be divided by a factor of 1.414, for a sech² pulse the factor is 1.543 to obtain the FWHM of the laser pulse. Asymmetric and complex pulse shapes cannot be measured since their shape gets lost (see bottom row in Figure 8). The autocorrelation always yields a symmetric trace.

The advantage of intensity autocorrelation is its easy implementation but if the exact pulse shape is not know it is not possible to determine the exact pulse length. Furthermore information about the phase in frequency and time domain cannot be obtained. Therefore additional techniques have been developed, for example the spectral phase interferometry for direct electric field reconstruction (SPIDER) [19] and the frequency-resolved optical gating (FROG). Both can determine the complete electrical field of ultrashort laser pulses. In this work the FROG technique was used and therefore will be described next.

2.3.3 Frequency-Resolved Optical Gating (FROG)

The principle setup for this technique is the same as for the intensity autocorrelation except the photodetector is exchanged with a spectrometer used for detection (see Figure 9). At each time delay a spectrum is recorded instead of an intensity signal. This means that the FROG trace is in the frequency-time-domain and therefore includes time and frequency information [7].

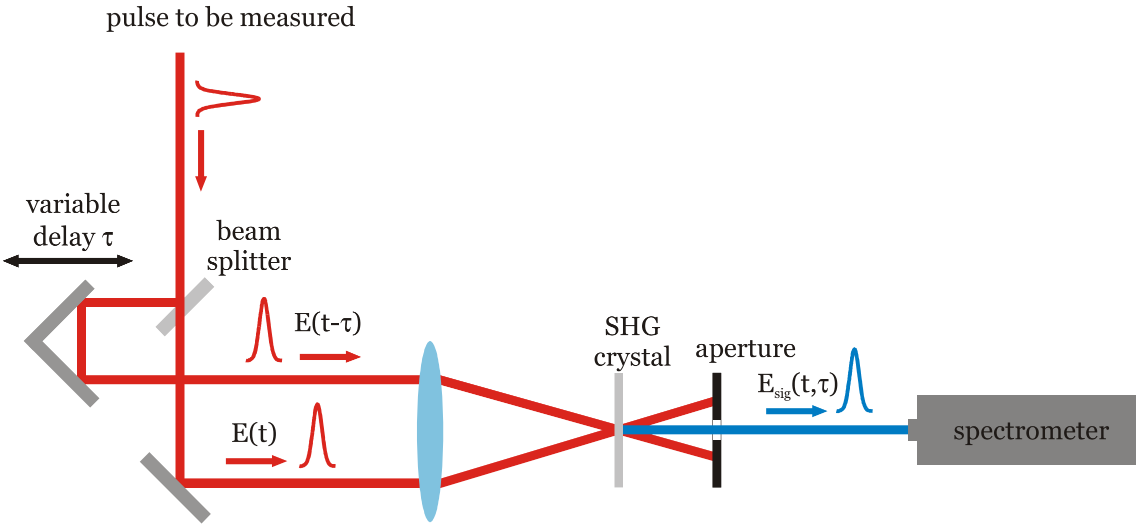

Figure 9: Setup for a FROG using second-harmonic generation

The amplitude and phase of the incident laser field *E(t)* are then retrieved from the FROG trace by using an iterative algorithm which is usually convergent in realistic cases. In an SHG FROG the spectrometer detects the intensity:

$$I_{FROG}^{SHG}(\omega,\tau)=\left|\int_{-\infty}^{\infty}E(t)E(t-\tau)\cdot e^{-i\omega t}dt\right|^{2} \tag{13}$$

The FROG measures the complete intensity and phase dependent on time and frequency with two exceptions. It cannot measure the absolute phase φ_0 and the pulse arrival time which corresponds to φ_1. There are also different variations of the FROG geometries for example the PG FROG (polarization-gate) and the THG FROG (third harmonic generation). The main advantage of the SHG FROG is its sensitivity. It involves only a second order nonlinearity which yields stronger signals than the third order effects.

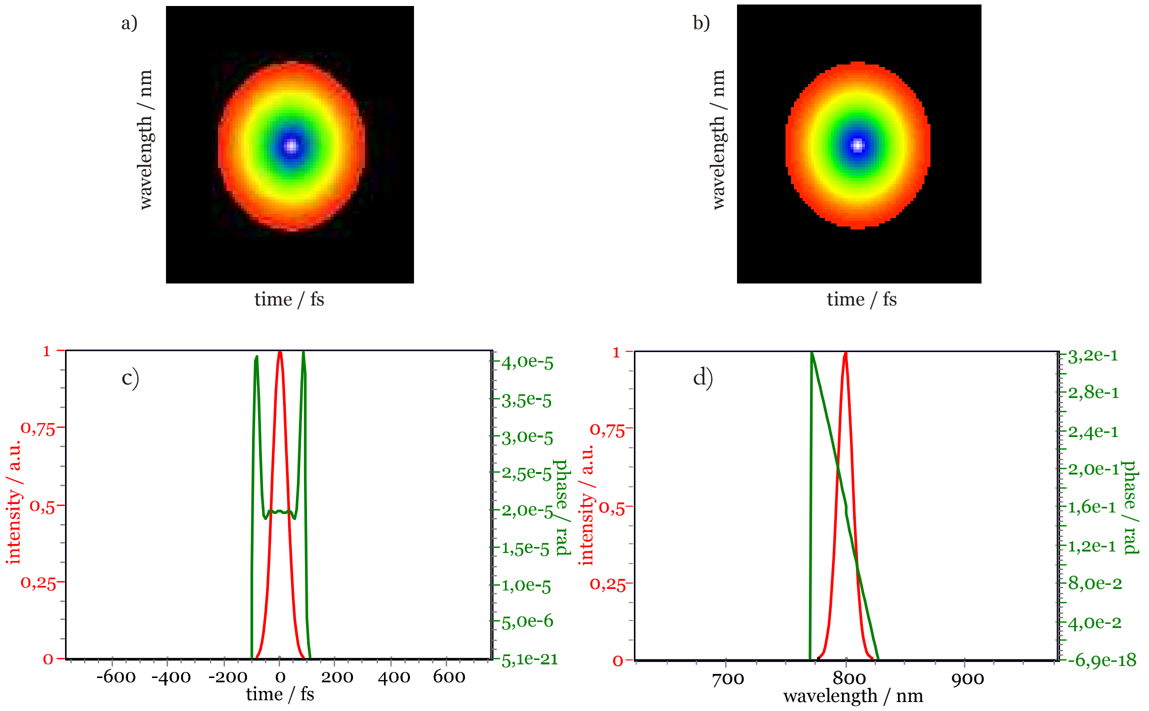

Figure 10: a) FROG trace of an ideal 60 fs pulse, b) retrieved trace, c) retrieved temporal pulse, d) and retrieved spectrum

In Figure 10 a FROG trace (a) of an ideal 60 fs Gaussian pulse is shown. After the iterative algorithm was applied an electric field (c) and frequency spectrum (d) were retrieved which results in a retrieved FROG trace shown in (b). As the pulse is ideal the phases should be flat. But it can be seen, that in time domain the phase is in the order of 10^{-5} radians and therefore practically zero. In frequency domain the phase is linear and therefore only corresponds to a time shift of the laser pulse and does not affect the pulse itself.

2.3.4 Beam Diameter Determination – Moving Edge

The fluence of the laser beam is a very important property. It is the energy per area and therefore the radius of the laser beam has to be determined. Laser beams can have different spatial beam profiles, e.g. the Ti:sapphire laser has a Gaussian beam profile. For determination one can use the “moving edge” method [3]. Figure 11 shows the scheme of the setup. The razor blade is scanned through the focus area and the transmitted energy for each position is recorded with a detector.

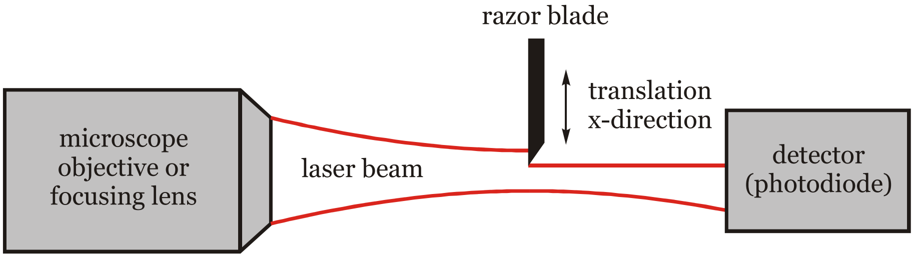

Figure 11: Scheme of the "moving edge" determining the beam radius

As the beam profile is Gaussian in x- and y-direction the fluence distribution *F(x, y)* can be described as

$$F(x,y) = F_0 \cdot e^{-\frac{2}{w_0^2}\cdot\left(x^2+y^2\right)} \tag{14}$$

where F_0 is the maximum fluence and w_0 is the beam radius. By definition the fluence *F(x,y)* has decreased to F_0/e^2 at the radius w_0. Calculating the transmitted energy E_T depending on the position of the razor blade yields [3]

$$E_T(x=l) = F_0 \cdot \sqrt{\frac{\pi}{2}} \cdot w_0 \cdot \int_l^\infty e^{-2\cdot\left(\frac{x}{w_0}\right)^2} dx \tag{15}$$

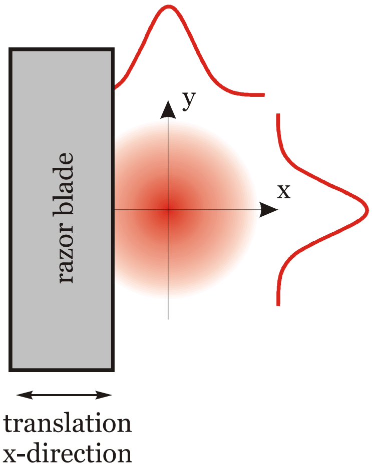

Figure 12: Perspective of the photodiode for the "moving edge" measurement

With this equation the numerical data can be fitted and the beam radius can be obtained.

2.4 Pulse Modification

Everything that changes the laser pulse, e.g. in intensity or phase in either time or frequency domain, is a pulse modification. One modification was described in chapter 2.2.3 where the goal was the compression of the pulse. But also the dispersion of glass is a modification. If someone wants more control over the pulse modification there is need of an additional device.

2.4.1 Pulse Shaper

Pulses directly from laser oscillators commonly have a Gaussian or sech^2 shape. But there is a large interest in waveform synthesis (or pulse shaping) to receive user defined pulse shapes or to control an experiment in a way to maximize the effort by finding an appropriate pulse shape. A very common method is the spatial masking of the spatially dispersed frequency spectrum of the laser pulse. As the time and frequency domains are related through the Fourier transformation changes in the frequency domain will affect the time domain. Therefore the description for pulse shaping can be made in both domains (see Figure 13). For the relation between input and output linear, time-invariant filters are used which describe the response between input and output.

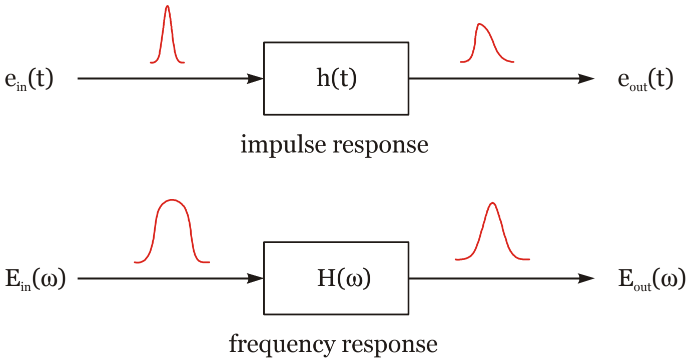

Figure 13: Transfer function in time and frequency domain

In time domain the output pulse $e_{out}(t)$ can be described as the convolution of the input pulse $e_{in}(t)$ and the impulse response function $h(t)$ [20].

$$e_{out}(t) = e_{in}(t) * h(t) = \int dt' e_{in}(t')h(t-t') \tag{16}$$

In the frequency domain the output $E_{out}(\omega)$ is the product of the input signal $E_{in}(\omega)$ and the frequency response function $H(\omega)$

$$E_{out}(\omega) = E_{in}(\omega)H(\omega) \tag{17}$$

The relation between *H(ω)* and *h(t)* can be described by the Fourier transformation

$$H(\omega) = \int dt\ h(t)e^{-i\omega t} \tag{18}$$

and

$$h(t) = \frac{1}{2\pi}\int d\omega\ H(\omega)e^{i\omega t} \tag{19}$$

Equation (18) is used to get the frequency response function for a desired time response. The control of the frequency domain of ultrashort pulses is much easier than the control of the time domain which is in the femtosecond regime. The principle setup of this pulse shaping technique is shown in Figure 14. It consists of a pair of gratings and lenses, and a pulse shaping mask. Without the mask the setup is known as “zero dispersion compressor” which means the input laser pulse will remain unchanged when passing the setup. The frequency components of the incident laser pulse will be angularly dispersed by the first grating and then focused by the first lens with the focal length f to the back focal plane which is the Fourier plane. At this plane the frequency components are spatially separated. The first lens performs the Fourier transformation of the angular dispersion from the grating to the spatial separation. The separated frequency components can be changed by an amplitude and/or a phase mask. After the manipulation the components are again recombined through the second lens and grating to a single beam. A shaped output pulse depending on the mask is received.

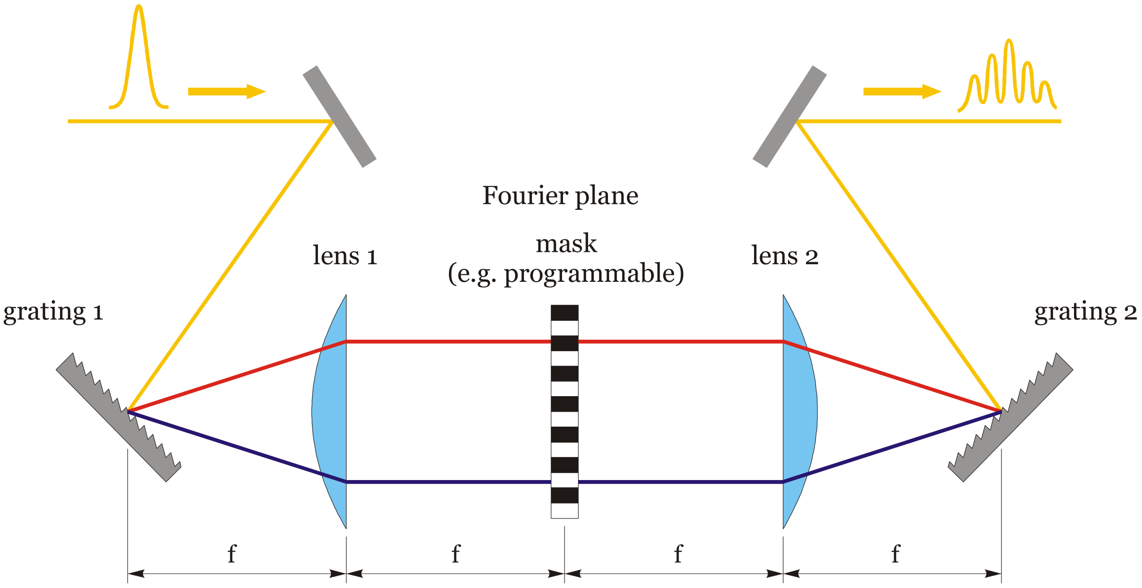

Figure 14: Setup scheme of a pulse shaper

The mask can be build up through fixed masks or programmable masks like the LC-SLMs (liquid crystal spatial light modulator). Using fixed masks provides excellent pulse shaping quality but it is not easy to provide continuous phase variations whereas binary phases work well. With a LC-SLM the continuous change of the phase and/or amplitude for each separate pixel is possible at the same time. It is also possible to change the mask and therefore the output pulse shape within 100 ms and less.

In principle the pulse shaper can be operated in two modes namely with and without feedback from the experiment. Without the feedback (Figure 15a) the knowledge of the input pulse as well as the output pulse has to be available. Therefore the mask can be calculated and applied to the display. This open loop configuration needs a good calibration of the LC-SLM to provide exact translation of the theoretically calculated mask to the physical device.

The programmable LC display offers the possibility of a feedback controlled system (Figure 15b) which is also called adaptive pulse shaping. The computer starts the experiment with a random mask and updates it according to the algorithm and the current state of the experiment. With this strategy the mask is optimized until the experiment is in the desired state. It is possible to remove a chirp of the input pulse [21] as well as the control of chemical reactions [22]. The only requirement for the closed loop control is a measurable optimization parameter which is directly fed to the computer. In adaptive pulse shaping the knowledge of the input pulse as well as the output pulse is not necessary. There is also no need to calibrate the SLM like in open loop control. The only requirement is the specification of the experimental outcome to be optimized and the algorithm for optimizing.

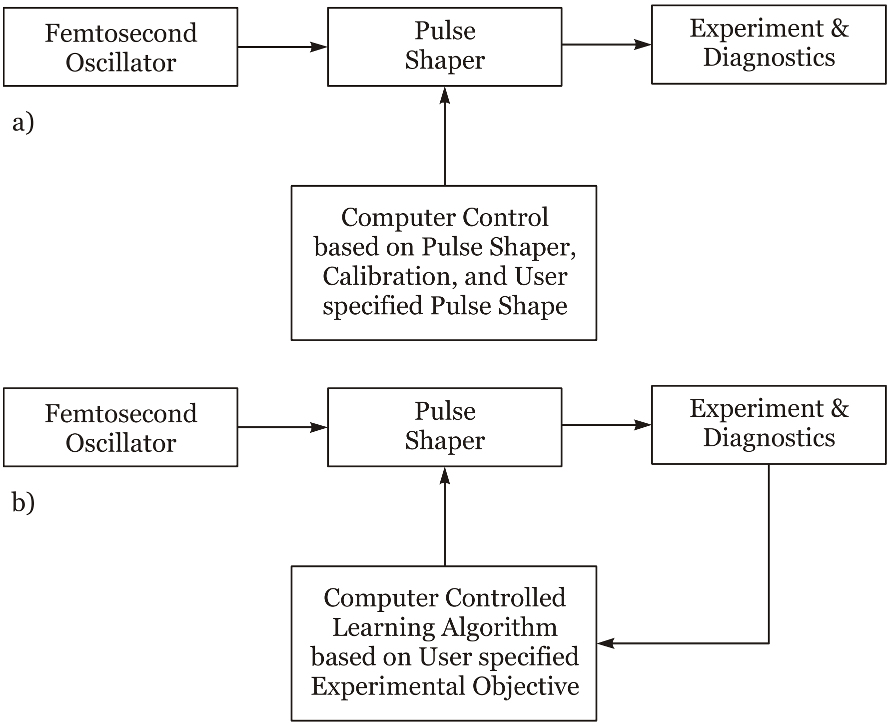

Figure 15: Experiment setup with a pulse shaper a) without and b) with feedback control

As it is possible to generate complicate pulses there is need of good characterization measurement techniques. The intensity autocorrelation is useless as it cannot recover the pulse shape appropriately. Therefore FROG is a method which is good known and can recover intensity and phase vs. time.

2.5 Inverse Pulsed Laser Deposition (IPLD)

In the experiments described later thin films were processed. Therefore the production method will be shortly described in the following section.

Pulsed laser deposition is a well known method for growing thin films [23]. Several geometries were proposed to get even more homogeneous films. One arrangement is the inverse pulsed laser deposition [24, 25] which is shown in Figure 16. The whole arrangement is inside a vacuum chamber for evacuation and then pure gas e.g. argon or nitrogen is introduced. If there is no inert gas the plasma will react with the oxygen in air.

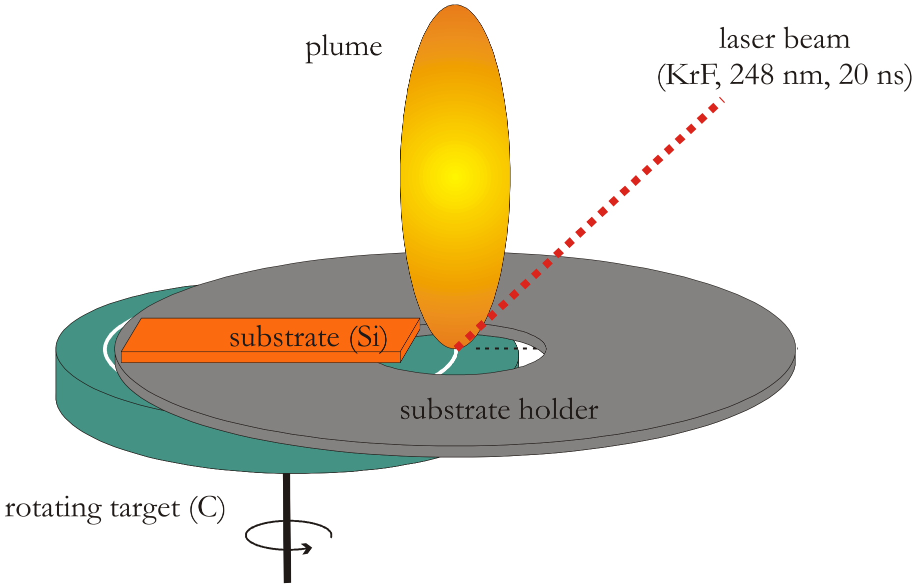

Figure 16: IPLD geometry for growing thin films

The high power pulsed laser beam is focused onto the target of the desired composition. The target material is vaporized and ejected in form of a plume. The backward motion of the plasma particles is used for growing the thin film. In the original PLD configuration the substrate is above the plume and faces it [23]. As the substrate is static this results in a decreasing film thickness on the substrate with increasing distance from the ablated laser spot. In comparison to the PLD configuration improved surface quality and higher deposition rates in the high-pressure domain are reported [25].

3 Experimental

3.1 Laser Setup

The general setup is shown in Figure 17 as a flow chart with black boxes for the different functionalities for an easy description of the “light flow”.

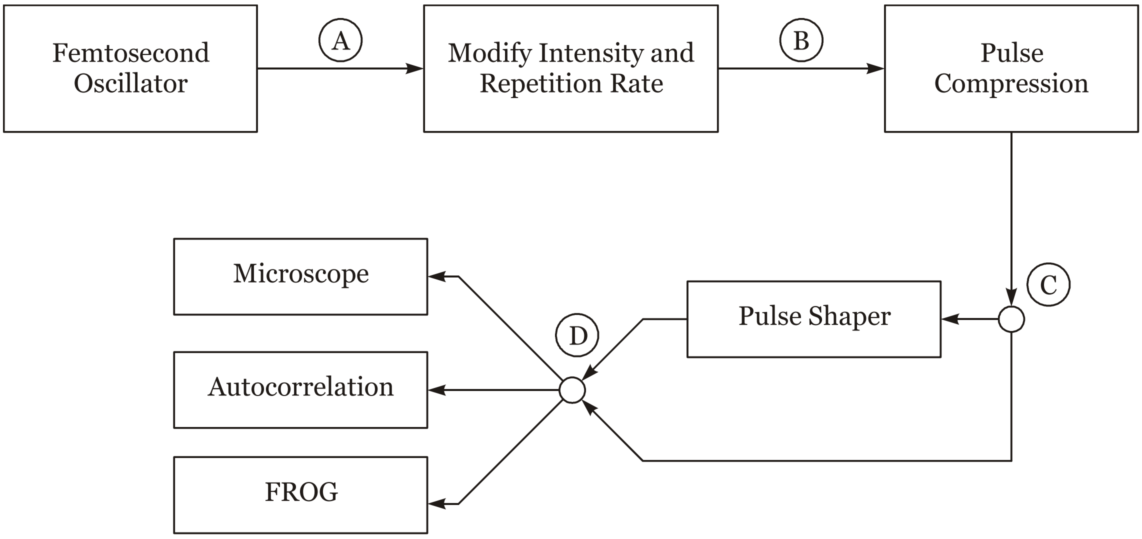

Figure 17: General setup scheme (light flow) used for the experiments

The laser pulses were generated with a Ti:sapphire oscillator (Scientific XXL Femtosource from Femtolasers) which have a pulse length of 60 fs at FWHM (in fact at point C after the compression), a repetition rate of 11 MHz, a centre wavelength of 800 nm and a average power of about 2.3 W. This results in high pulse energies (>200 nJ directly after the oscillator) which can only be reached due to positive chirped pulse generation used inside the oscillator (pulse length of a few ps). The optical path of the laser beam inside the oscillator is shown in Figure 18. The pump source for the Ti:sapphire crystal is a diode pumped frequency doubled $Nd:YVO_4$ continuous wave laser (Coherent Verdi V18) with a centre wavelength of 532 nm and a maximum power of 18 W. In the experiments the Ti:sapphire crystal is only pumped with a power of 13.5 W. The short cavity arm is terminated with a SBR (saturable Bragg reflector) for mode locking. The long cavity arm is extended with a Harriot cell [26] to get high energy pulses. The laser pulses are reflected eight times on each of the two mirrors of the Harriot cell which results in an optical path of several meters. After the output coupler, which terminates the long cavity arm, the spot size is enlarged using a 1:2 telescope consisting of two lenses. The average output power of the oscillator is in the range of 2.3 W which is measured with a powermeter (Spectra-Physics model 407A) at point A marked in Figure 17. At the same point the frequency spectrum is checked continuously during the experiments with a spectrometer (Ocean Optics USB4000) because a deviation in the spectrum leads to different pulse lengths.

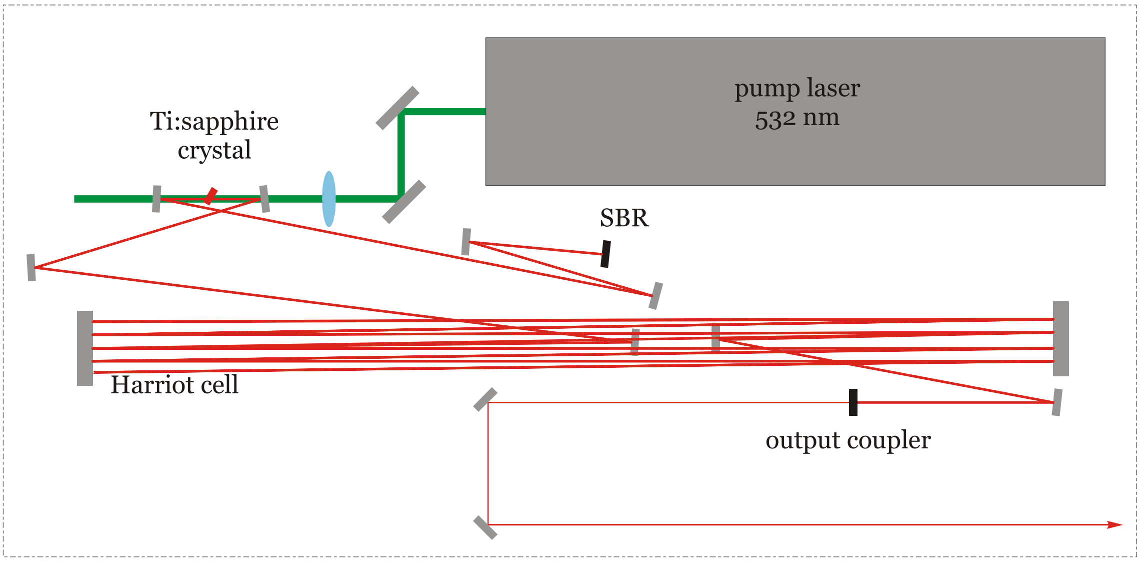

Figure 18: Setup of a Ti:sapphire high power fs-laser

The pulses intensity and repetition rate can be modified in the second part. For changing the light intensity a λ/2-plate, which changes the plane of polarization, in combination with a polarizer is used. The repetition rate can be changed from 5 Hz to 5 kHz with a Pockels cell and two crossed polarizers. In the third part the positively chirped pulses from the oscillator were compressed with a prism compressor using a two prism arrangement. Care must be taken not to clip a part of the dispersed beam which results in a clipped frequency spectrum. The spectrum has to be checked at point C marked in Figure 17 and has to be the same as at point A. After the prism compression (point C) the laser pulse has the desired properties, e.g. energy, pulse length and repetition rate. Because of the light absorption of the Pockels cell and the prism compression the pulse energy has a maximum value of 150 nJ at point C. These pulses can directly go to point D where the laser pulses can be characterized with the autocorrelation or the FROG or the pulses can be used for the experiments under the microscope. But it is also possible to go from C to D through the pulse shaper to modify the pulses shape and characterize these pulses and carry out experiments. The different optical light paths can be set by a flip mirrors.

The autocorrelator and the FROG use the same physical setup. The principle method is based on the second harmonic generation using a BBO crystal (β-barium borate) using a non-collinear setup. For the autocorrelation the intensity is detected with a photodiode detector and for the FROG the photodiode is exchanged with a spectrometer (Ocean Optics USB4000) capturing the spectrum of the frequency doubled signal. The necessary time delay is produced by a computer controlled translation stage (PI M405.DG Precision Translation Stage). The program used for measuring the autocorrelation is written in LabVIEW (Version 8.5) which allows a full automatic continuous acquisition of the laser pulse width. One autocorrelation diagram can be measured within half a second. As described in chapter 2.3.2 the pulse shape has to be known to calculate the pulse length from the autocorrelation length. The LabVIEW program uses a factor of 1.41, e.g. a Gaussian pulse shape is taken, to convert the autocorrelation length. The pulse length is the FWHM. During the experiments the pulse length is checked continuously to guarantee constant experimental conditions. For complete determination of the intensity and phase of the pulses FROG is used. The current version of the LabVIEW program captures a defined number of spectra at different time delays, extracts the data around the second harmonic frequency and stores the data in a file. This file can be read with the Femtosoft FROG3 software [27] to retrieve intensity and phase of the laser pulse. As the data measurement and retrieval process are two different programs, the acquisition is not continuously and also lasts much longer then the autocorrelation acquisition.

Microscope

The moving edge and ablation experiments were made using a microscope. With the used microscope Axio Imager.M1 from Zeiss it is possible to couple the laser beam through the objective and focus the laser beam onto the sample. As the laser pulses go through glass in the objectives the pulses will be linearly dispersed. Therefore chirped mirrors, which are designed to compensate the dispersions of the used Zeiss objectives, are settled into the beam. Additional care has been taken by measuring the pulse energy because not all energy at the input of the microscope is measured after the objective. A factor has been calculated to get the energy of the pulses directly at the experiments depending on the input energy.

Moving Edge

The razor blade is mounted on an object holder and moved with the microscope translation stage. For measuring the transmitted light a photodiode connected to the oscilloscope is used. The focus is set to the sharp edge of the razor blade. As the laser spot is very small and therefore the fluence is very high the laser power has to be reduced to avoid destruction of the razor blade. Then the razor blade is scanned stepwise through the focus and the voltage corresponding to the transmitted light is recorded.

Laser / System	FEMTOSOURCE scientific XL (Ti:Sapphire)
Pump Source	COHERENT Verdi V18 532 nm 18 W
	Nominal Pulse Length: 60 fs (after compression)
	Centre Wavelength: 800 nm
	Repetition Rate: 11 MHz
	Average Output Power @ 11 MHz: 2.3 W
	Pulse Energy: >200 nJ
Pockels Cell	
Head / Crystal	Bergmann ds11b/KD*P
Control Unit	Femtolasers Frequency Power Control (Model: FPC Type: XL)
Timing Unit	Bergmann Bme-PTO2
Pockels Cell Driver (high voltage generation)	Bergmann PCD3i
Powermeter	OPHIR NOVA DISPLAY + PD10-PJ-SH-V2
Powermeter	Spectra-Physics model 407A
Microscope	ZEISS Axio Imager.M1
Digital Camera	AxioCam MRc5
	Axio Vision Rel. 4.7 (Software)
Objectives	Zeiss EC „Plan-Neofluar“ 10x0,3 M27
	Zeiss EC „Plan-Neofluar“ 20x0,5 M27
	Zeiss EC „Plan-Neofluar“ 40x0,75 M27
	Zeiss LD EC „Plan-Neofluar“ 63x0,75 Korr M27
	Zeiss LD EC „Epiplan-Neofluar“ 100x0,75 DIC M27
Oscilloscope	LeCroy WaveRunner 64Xi 600 MHz 10 GS/s
Pulse Shaper	Setup like used at the University of Kassel
LCM	CRI SPATIAL LIGHT MODULATOR SLM-640-P controlled via LabVIEW
Data Acquisition Board	NI USB-6221
Micrometer Stages	PI M-405.DG Precision Translation Stage
Controller	PI C-848.43 Digital DC-Servo-Motor Controller
Spectrometers	Ocean Optics USB4000-UV-VIS
	Ocean Optics USB4000-VIS-NIR
Software	Ocean Optics SpectraSuite + OmniDriverSPAM 2008.05.29
Atomic Force Microscope (AFM)	NT-MDT NTEGTA Aura
	100x100 µm Scanner
LabVIEW	Version 8.5
Frog Retrieval Software	Femtosoft Technologies FROG 3.2.2

Table 1: Equipment and software used for experiments

Pockels Cell

The physical setup of the used Pockels cell consists of four different parts. The main part is the head with the crystal KD*P (potassium dideuterium phosphate) utilizing the Pockels effect [10]. The second part is the high voltage unit (Bergman BCD3i) which drives the crystal. A voltage of about 7 kV is necessary to turn the plane of light 90°. It is a challenging task for the electronic part to apply this voltage within a few nanoseconds. Care has to be taken if very sensitive measurements are made in the surroundings because the electromagnetic field of the high voltage unit of the Pockels cell induces current in other electronic circuits and wires which results in systematic faults. The control unit (Femtolasers Frequency Power Control, Model: FPC, Type: XL) is used for setting the number of transmitted pulses and the repetition rate. The timing unit (Bergmann Bme-PTO2) uses the information of the control unit and generates the switching functions for the high voltage unit. To synchronize the timing unit to the pulse train the latter is measured with a photodiode at point A marked in Figure 17. The timing unit generates two signals which control the high voltage unit and therefore switch on and off the high voltage.

3.2 Ablation Experiments

IPLD – Inverse Pulsed Laser Deposition

This method was used to create thin diamond-like carbon (DLC) films used for the ablation experiments. The preparation technique employed here results in tetrahedral amorphous carbon (ta-C) with sp^3 contents as high as ~80% [28]. Therefore the deposition chamber was first evacuated to a base pressure of $1.5–2.10^{-4}$ Pa by a turbo molecular pump, and then the pressure was increased to 5 Pa by introducing high-purity (99.999%) argon gas using a flow configuration. The graphite target, rotating at 10 rpm, was ablated at 10 Hz repetition rate by KrF laser pulses (248 nm, 20 ns) of 7 J/cm^2 fluence. The beam was focused by a 35 cm focal length UV grade fused silica lens onto an approximately 1 mm^2 area of the target surface at 45 degree angle of incidence. Observations described in [29] made it possible to characterize the lateral thickness distribution by means of measuring the changes in the film thickness along the two axes of the laser spot. In each experiment, films were collected on two, 8-mm wide polished silicon stripes, fixed right above the rotating target, at room temperature. The thickness distribution of the carbon layer was measured using profilometry and is shown in Figure 19. The production and characterization of the used films was done by the Department of Optics and Quantum Electronics at the University of Szeged.

Experiments

The ablation experiments were carried out under the microscope with the 63x Zeiss Neofluar objective with NA=0.75. Different combinations of pulse energies and numbers were used to create irradiated zones. The irradiated areas were inspected in situ in reflection mode and afterwards by a atomic force microscope (NTEGRA AURA) in contact mode.

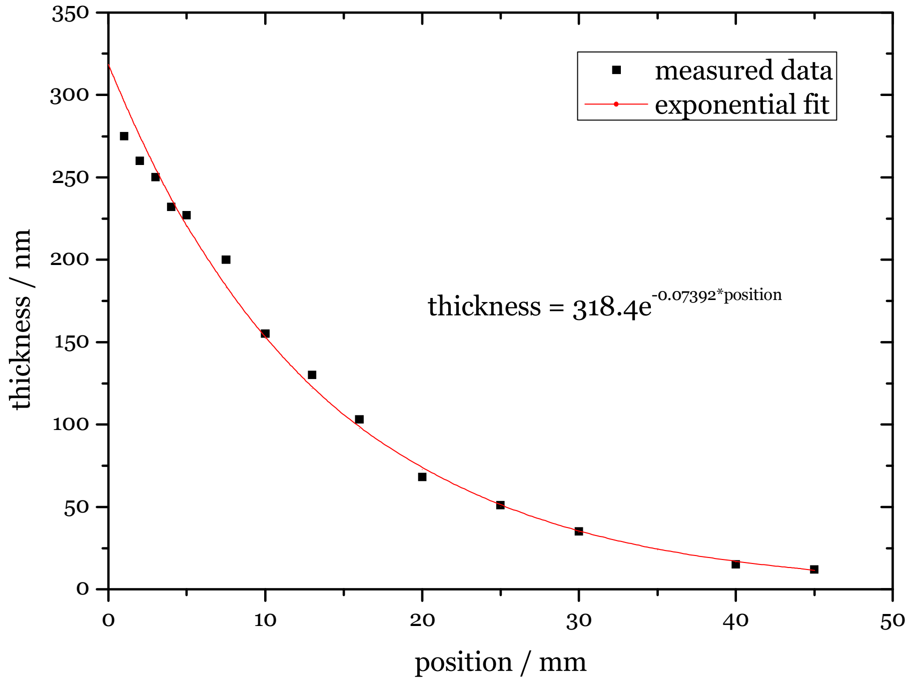

Figure 19: Thickness profile of the thin film used for the ablation experiments

4 Results and Discussion

4.1 Pulse Characterization

Every day the output power and the pulse length are checked several times because the long time stability is affected by the high energy regime mode. In Figure 21 a sample autocorrelation of the optimized system without the pulse shaper is shown. The measured data are fitted with a Gaussian shape and then the pulse length is determined. At low intensities the measured data deviate from the ideal Gauss shape depending on the degree of optimization of the laser. Therefore in the online measurement system (see appendix) two data fits are made. The first uses the whole dataset to fit a Gaussian shape into the pulse and the second fit only uses the intensities of the measured data points which are above 40 percent of the peak intensity (this value can easily be changed). For a well adjusted system this two fits are equal.

To get a well adjusted system the oscillator has to be optimized first. It is the goal to run the system always in the same state and therefore get the same properties of the laser pulses. There are three properties/parameters to check at the output of the oscillator. The first is the average output power of the oscillator which should be in the range of 2.3 W for this particular device. The second parameter is the frequency spectrum which is compared with a reference spectrum which was saved when the oscillator was optimized. A typical frequency spectrum generated from the oscillator is shown in Figure 20. Finally the spatial shape of the laser pulse is checked because it is possible to get a spatial shape deviating from a Gaussian. There are two main parameters to optimize the oscillator namely the stability range which changes the length of the short cavity arm and the second is the input coupling of the pump laser.

At the output of the oscillator the laser pulses are dispersed and the prism compression has to be adjusted to get short pulses after the compression. Therefore the position of the second prism is changed as described in the theoretical part to introduce more or less negative dispersion. For the pulse length measurement the autocorrelation is used for daily use but also FROG traces were taken to check the phases. The following figures show the typical output of the laser oscillator characterized by the spectrometer (Figure 20), the autocorrelation (Figure 21), and the FROG (Figure 22). The pulse duration measured with the autocorrelation was 58 fs.

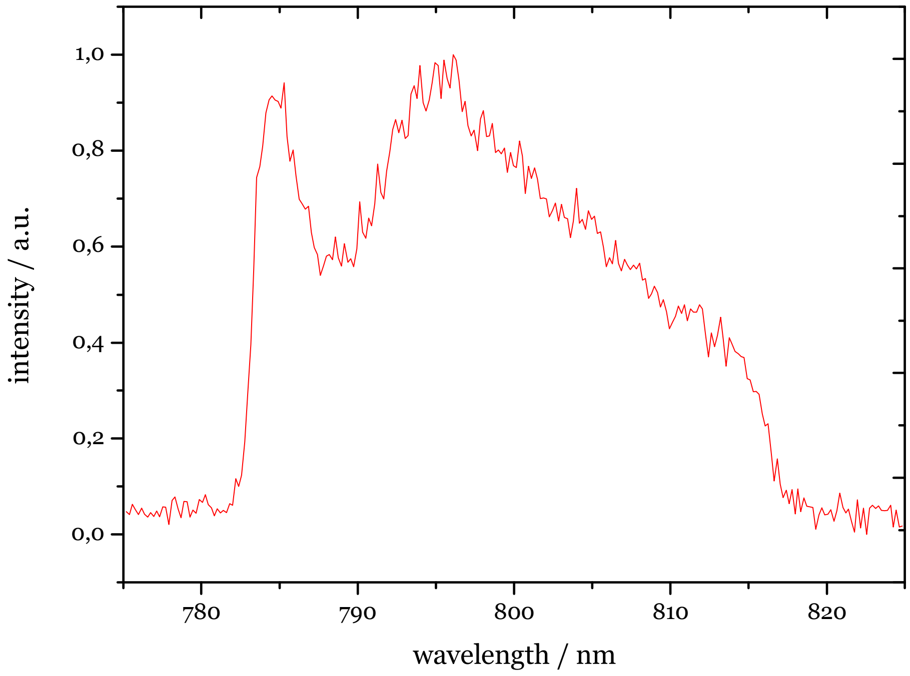

Figure 20: Spectrum of a 58 fs laser pulse of the FEMTOSOURCE scientific XL oscillator

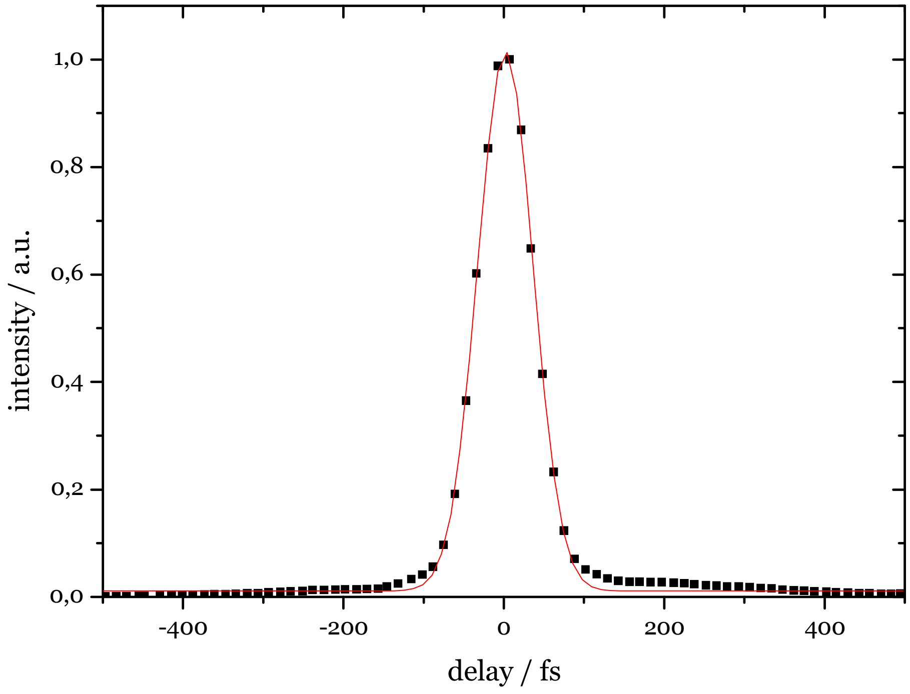

Figure 21: Intensity autocorrelation of a 58 fs laser pulse of the FEMTOSOURCE scientific XL oscillator

The pulse duration was compared with the FROG result which yielded a pulse length of 59 fs. In addition the FROG trace shows the temporal and spectral phase and it can be seen that it is not flat and therefore the pulses are not Fourier-limited. Looking at the scale of the phases one may assumes a large phase. But the effective phase is about 1.5 radians (~0.5π) because the shown phase only affects the pulse if the intensity is not zero. The retrieved frequency spectrum is slightly different from the one in Figure 20. The reason may be the calibration of the spectrometer necessary for the recalculation of the original spectrum from the second harmonic spectrum.

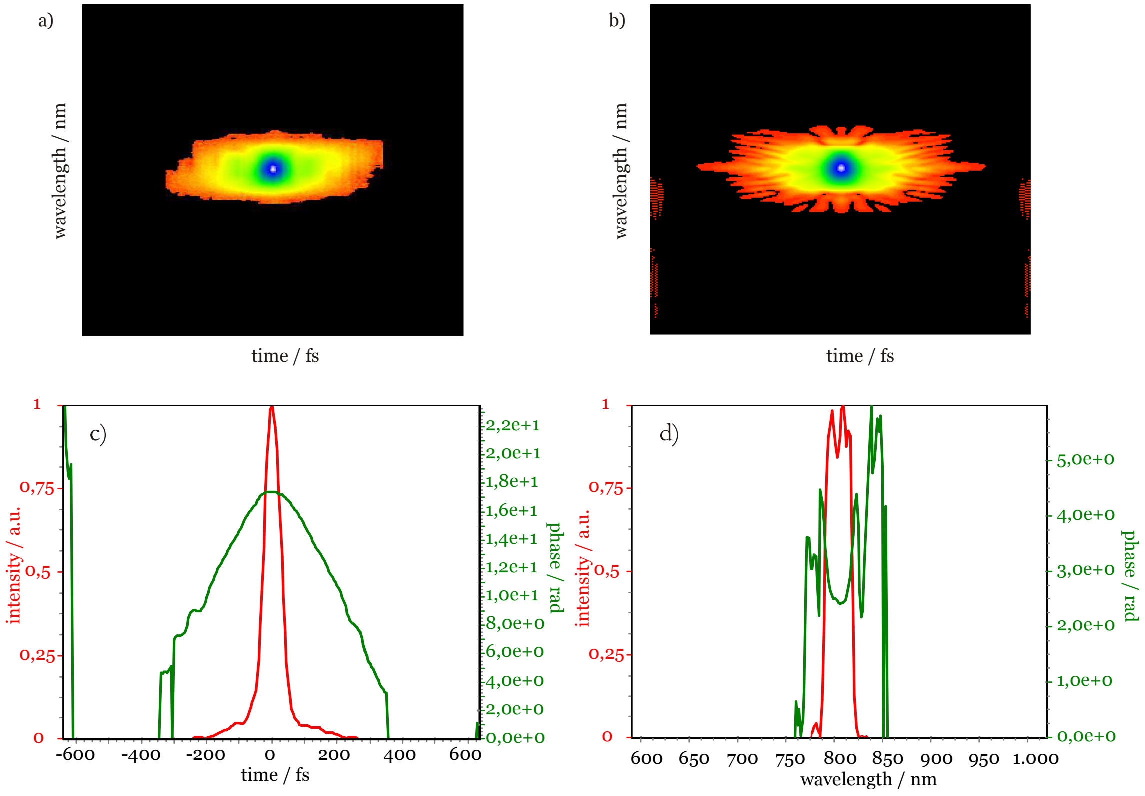

Figure 22: FROG analyses of the fs-laser pulse a) measured and b) retrieved trace c) retrieved electric field and d) retrieved frequency domain

4.2 Microscope Objective Characterization

4.2.1 Beam Diameter – “Moving Edge” Method

This method is used to determine the laser beam radius at the focus of the microscope objectives. With the knowledge of the radius and the pulse energy the fluence can be calculated which is the crucial parameter for material ablation treated in the experiments.

The measured data were fitted with Origin 8.0. The program does not support user defined fitting functions with an integral as described in equation (15) which was retrieved in the theoretical section. Thus the integral has to be solved to get a fitting function usable in Origin. First the boundaries of the integral need to be changed because all experiments start with zero light intensity moving to maximum intensity and therefore the transmitted light has to be integrated from -∞ to the actual position l

$$E_T(x=l) = F_0 \cdot \sqrt{\frac{\pi}{2}} \cdot w_0 \cdot \int_{-\infty}^{l} e^{-2\cdot\left(\frac{x}{w_0}\right)^2} dx \tag{20}$$

Integrating this equation yields

$$\begin{aligned} E_T(x) &= F_0 \cdot \frac{\pi}{4} \cdot w_0^2 \cdot \left[1 + erf\left(\sqrt{2} \cdot \frac{x}{w_0}\right)\right] + C \\ &= F_0 \cdot \frac{\pi}{4} \cdot w_0^2 + C + F_0 \cdot \frac{\pi}{4} \cdot w_0^2 \cdot erf\left(\sqrt{2} \cdot \frac{x}{w_0}\right) \end{aligned} \tag{21}$$

for $w_0 > 0$

For the final fitting function the first two constant parts of equation (21) are replaced by y_o and an offset variable x_o in x-direction is introduced to allow a shift of the data in x-direction.

$$y = y_0 + F_0 \cdot \frac{\pi}{4} \cdot w_0^2 \cdot erf\left(\sqrt{2} \cdot \frac{x - x_0}{w_0}\right) \tag{22}$$

It can be seen that the measured data fit very well to the Gaussian shape (Figure 23).

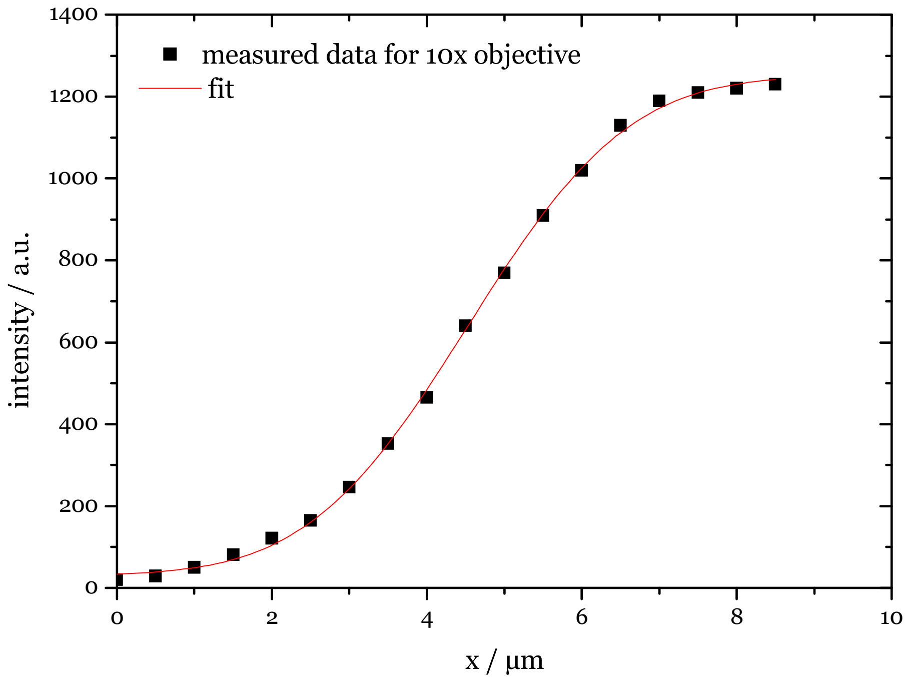

Figure 23: Dataset and fit for the laser beam radius of the 10x objective

The results for all objectives are shown in Table 1. It can be seen that the higher the numerical aperture of the objective the smaller is the beam radius in the focus which corresponds to the resolution of the objective. Objectives with the same numerical aperture show nearly the same beam radius.

Objective	Numerical aperture NA	Beam radius w_0 / µm
10x	0.3	3.4
20x	0.5	1.8
40x	0.75	1.1
63x	0.75	1.2
100x	0.75	1.0

Table 2: Beam radius at the focus of different objectives measured with the moving edge method

4.2.2 Determination of the Group Velocity Dispersion

The objectives introduce dispersions because of the lenses inside which results in a broadening of the laser pulses. To compensate the dispersions chirped mirrors are used. The measurement of the autocorrelation of the laser pulses passing the chirped mirrors and the objective showed that the dispersion can be compensated and therefore the pulse length of the input and output pulse is the same.

4.3 Pulse Shaper

Substantial attention and time was spent for the assembling and characterization of the femtosecond pulse shaper. The setup of the pulse shaper relies on the construction plans of Jens Köhler (University of Kassel). It is designed for fs-lasers with a centre wavelength of 800 nm, a maximum spectral width of 90 nm (base width and not FWHM), and a maximum beam diameter of 5 mm. The LC-SLM is a 640 pixel phase only modulator.

In Figure 24, the top view of the pulse shaper with its main components, which are listed in Table 3, is depicted. The height of the input and output beam is about 9.5 inches and is changed to the nominal height of 2 inches of the laser beam in our setup due to periscopes which are not shown.

Optical path

The optical path (Figure 24) runs along the components 1 to 11. The plane of the light between the parts 4 to 8 is parallel to the ground plate to provide a normal incidence to the SLM (part 6). The length of the optical path between the gratings 3 and 9 should be four times the focal length of the cylindrical mirrors 2 and 10. At the centre, the SLM introduces phase shifts in the spatially dispersed frequency space (= Fourier plane).

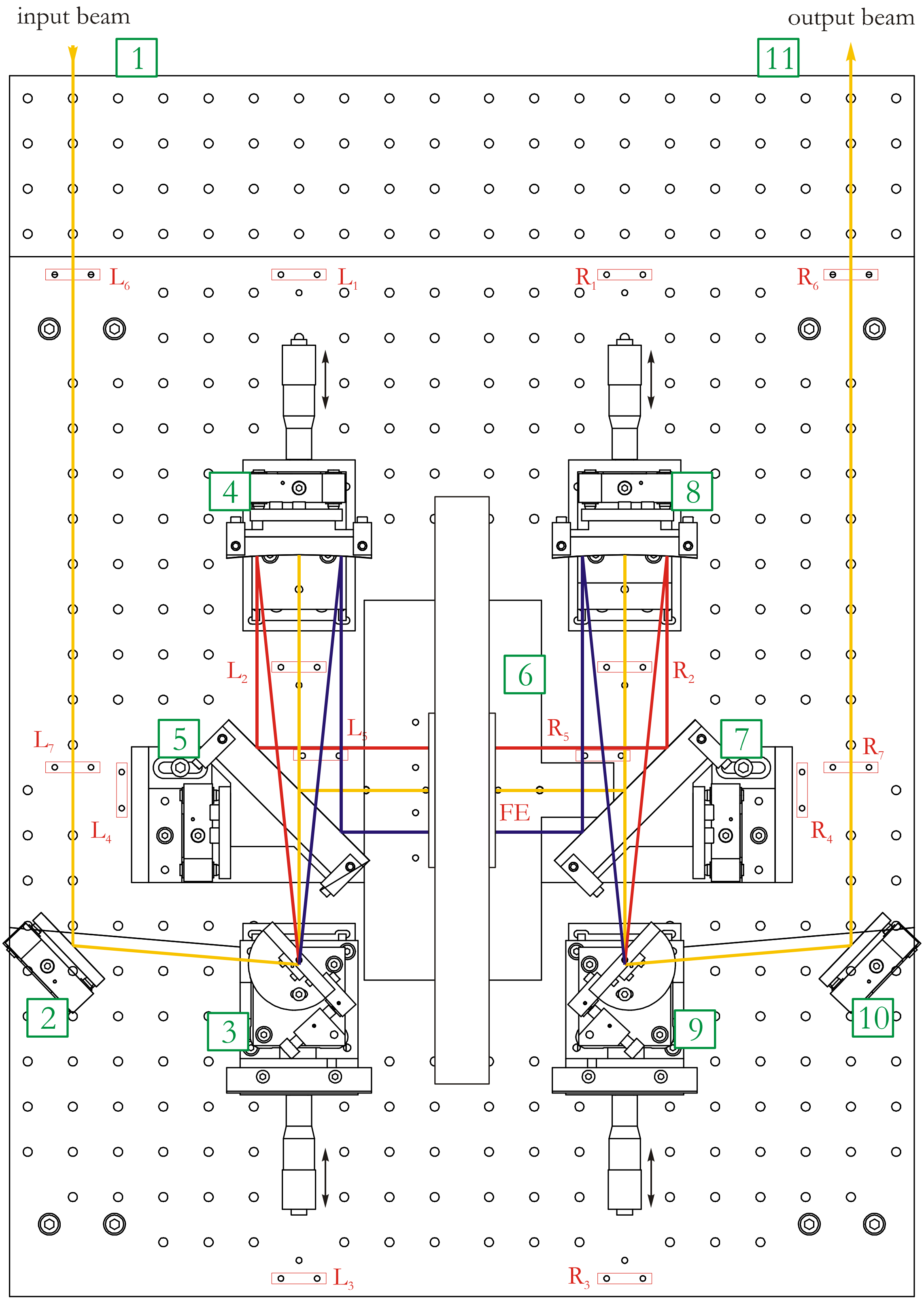

Figure 24: Top view of the pulse shaper

Parts

Part No.	Description
1 + 11	Periscopes to change beam height from 2 to 9.5 inches
2 + 10	Mirrors for input and output coupling
3 + 9	Gratings, Wasatch Photonics, Dickson® 1840 lpmm Volume Phase Holographic (VPH) Transmission Grating for 800 nm
4 + 8	Cylindrical mirrors, f = 220 mm, BK7, silver coated, size 80x20 mm
5 + 7	Plane mirrors, BK7, silver coated, size 110x20x20 mm
6	Liquid Crystal Spatial Light Modulator LC-SLM CRi SLM-640-P

Table 3: Optical parts of the pulse shaper

A precise alignment of the pulse shaper is necessary in order not to introduce dispersions. It is the goal that a defined input pulse should not change its properties by passing the pulse shaper setup. There is a summary of the alignment steps done for the pulse shaper. A complete technical documentation with the drawings of all parts and more detailed adjustment documentation is available [30].

Alignment Steps

There are different apertures with different heights and aperture sizes and there are some further utilities for the correct alignment of the laser beam in the pulse shaper. They are listed in Table 4. All optical components can be easily removed to align the laser beam along the apertures and then added precisely again.

Part No.	Description
1	124.0 mm HeNe-aperture
2	132.5 mm reticule for the left side
3	132.5 mm reticule for the right side
4	Screen for the Fourier plane
5	139.3 mm fs-laser-aperture
6	Optical mount simulator
7	Iris apertures
8	Variable height apertures

Table 4: List of apertures and utilities for laser beam alignment

- First of all the convolution mirrors have to be aligned. The beam reflected from the left cylindrical mirror is reflected orthogonally from the left convolution mirror and further reflected orthogonally from the right convolution mirror to the right cylindrical mirror. The plane of the beam between these parts has to be in parallel to the ground plate. Therefore a HeNe-laser beam is adjusted to go through 124.0 mm HeNe-apertures from L_1 to L_2 to L_3. The left convolution mirror is added and has to be aligned in a way that the reflected beam passes the apertures at positions FE and R_4. The right convolution mirror is added too and aligned in a way that the reflected beam passes the apertures at the positions R_2 and R_1.

- The second part is the horizontal, vertical, and rotational adjustment of the cylindrical mirrors. Therefore a HeNe-laser beam is adjusted with 124.0 mm HeNe-apertures along the positions R_1 to R_2 to R_3. The beam is reflected from the right to the left convolution mirror and then to the cylindrical mirror. The cylindrical mirror has to be aligned in a way that the beam is self-reflected. The rotation of the left cylindrical mirror has to be aligned in a way that the profile of the reflected divergent beam is horizontally.
- Next the vertical adjustment of the reflected beam of the cylindrical mirror will be done. The 132.5 mm left reticule is added at position L_5. The vertical alignment of the left cylindrical mirror has to be changed until the reflected beam hits the centre of the reticule.
- Then a mirror is set into the left grating mount. The mount has to be adjusted in a way that the beam is self-reflected for the horizontal position and then vertically aligned to be parallel to the ground plate. The reflected beam is fixed with two iris apertures.
- The distance between the Fourier plane and the cylindrical mirrors should be one focal length. Hence two parallel beams are coupled into the setup in reverse direction using the installed iris apertures in the last step. The parallel beams hit the left cylindrical mirror and then are focused. The intersection point of the beams equals the focal point of the cylindrical mirror and so the position of the mirror is changed with the micrometer screw until the intersection point meets the Fourier plane (using the screen for the Fourier plane)
- As the position of the left cylindrical mirror has changed the vertical adjustment has to be repeated like 3 steps ago.
- The last five steps have to be done with all positions mirrored for the right cylindrical mirror.
- The parts setup until now should not change the beam profile. For this check the HeNe beam (with a good spatial beam profile) is coupled into the setup with the iris apertures installed before. The beam is reflected from the mirror in the grating mount, the cylindrical mirror, the convolution mirror and same at the mirrored side. The beams profile should be the same like without the setup at a

comparable distance. Otherwise the positions and the rotations of the cylindrical mirrors can be changed slightly.

- Next the tilt angle of the gratings is aligned. Thus the laser beam is aligned along the positions R_1, R_2, and R_3. The tilt angle of the mount of the left grating is aligned in a way that the beam is self-reflected. Same adjustment can be done for the mirrored side.
- At this point the first time the fs-laser beam is used. It is aligned with the 139.3 mm apertures along the points L_1 to L_2 to L_3. The former installed mirror is exchanged with the grating now. The optical mount of the left grating is exchanged with the optical mount simulator so that the gratings vertical axis is vertical orthogonal to the ground plate. The angle of the grating is approximately aligned 45° to the incident laser beam. The rotation of the grating is aligned in a way that the first order diffraction is horizontally, which can be checked in some distance. The plane of the first order diffraction and the input beam should be in a plane parallel to the optical table.
- Then the diffraction efficiency of the grating is maximized. It is easier to use an 800 nm non-mode-locked laser beam. The angle of the grating has to be changed until the power of the first order diffraction has its maximum. Then the optical mount simulator can be exchanged with the optical mount again.
- The last two steps have to be done for the right grating in the same manner.
- The principle geometrical alignment is ready and the input and output coupling has to be done.
- Therefore an 800 nm laser beam is aligned with the 124.0 mm HeNe-apertures along the positions R_1, R_2, and R_3. The position of the laser beam is fixed with iris apertures between the left grating and the convolution mirror and behind the left grating (the first order diffraction). The mirror left to the left grating is installed in a way that the beam is parallel to the ground plane and in the direction of the input periscope as shown in Figure 24. At the positions L_7 and L_6 the beam is fixed with variable height apertures.
- The fs-laser beam can be coupled into the pulse shaper like in the final state as shown in Figure 24. The output laser beam is also fixed with two iris apertures like on the left side and the mirror for the output coupling can be installed.
- To check the correct height of the beam in the Fourier plane the screen for this purpose is settled into the pulse shaper at position FE. The tilt angle of the

grating and the cylindrical mirror has to be changed in opposite direction to keep the plane of the spread spectrum parallel to the ground plane.

- The spatial chirp can be checked when the laser beam is watched in some distance and the spread beam is partially blocked in the Fourier plane. If there is a spatial chirp it can be removed by rotating or changing the angle of the right grating.
- There should not be a temporal chirp too. It is necessary that the pulse shaper is an exact 4f-setup. To check the temporal chirp the autocorrelation is one possibility but as it is not a complete characterization another method has to be used, e.g. FROG. To remove a possible chirp the positions of the cylindrical mirrors and the right grating can be changed slightly. The input pulse should be reconstructed without any change at the output when there is no light modulator in the Fourier plane – also called zero-dispersion compressor.
- The LC-SLM can be added to the setup and aligned to be in the centre. The introduced dispersion can be compensated through the change of the position of the cylindrical mirrors

Zero-Dispersion Compressor

The complete pulse shaper setup without the LC-SLM display is called zero-dispersion compressor which means that an input pulse should exit the pulse shaper without an additional dispersion. In the current setup the autocorrelation of a Gaussian 60 fs laser pulse leads to an autocorrelation trace shown in Figure 25.

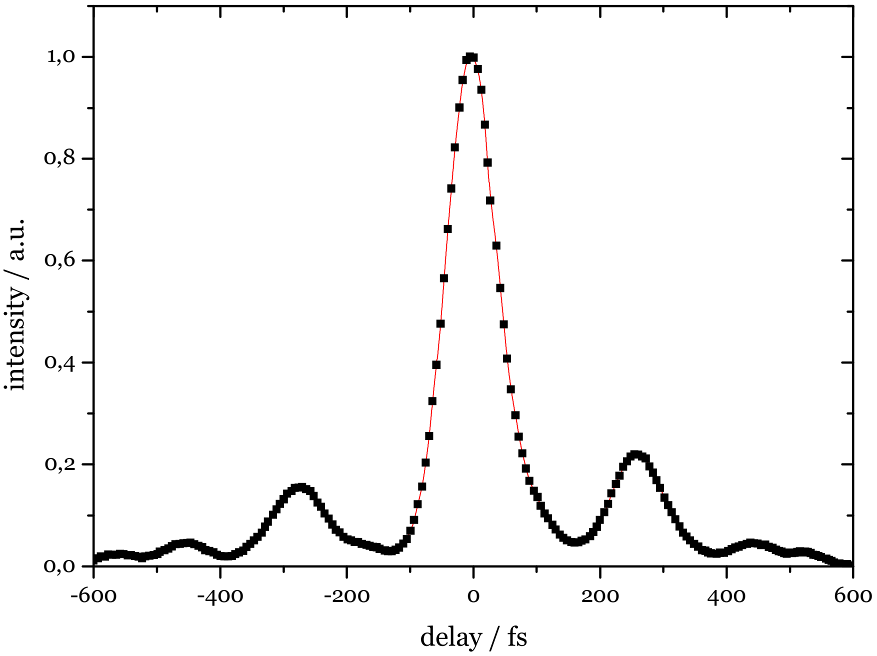

Figure 25: Autocorrelation of the laser pulse after passing the pulse shaper

It can be seen that the Gaussian pulse shape cannot be reconstructed. Up to now it is not clear if there is a misalignment or if one of the optical parts introduces changes in the phase or amplitude. Every change of the alignment of the gratings or mirrors led to a worse autocorrelation than the showed one. In principle such wings are due to third order dispersions which can only be introduced by the gratings in our setup. Many different settings were tried but none led to a perfect alignment. It should be noticed that the centre peak has a FWHM only a few fs greater than the input pulse and therefore the pulse shaper seems to be well aligned.

Absorption Losses

Next the losses inside the pulse shaper were checked. The developer of the pulse shaper specifies in his documentation that losses between input and output are less than 50 % but the measured loss is about 54 %. Table 5 shows the power measured at different positions in the pulse shaper and the relative losses for the components were calculated. It can be seen that the gratings have a loss greater than 20 % which is much more than the specified 13% at 800 nm shown in Figure 26. Also the mirrors have a substantial loss. Between the left grating and the Fourier plane the loss is 16 % which corresponds to the metallic cylindrical and metallic convolution mirror. This results in a loss of power by 8 % per mirror. The vendor specifies a reflectivity for his metallic mirrors greater than 96 % [31] whereas our mirrors have a reflectivity of about 92 %. Also the metallic mirrors on the right side have a greater loss than the specified one. The theoretical loss of the pulse shaper without the LC-SLM is

$$Loss(\%) = (1 - 0.87 \cdot 0.96 \cdot 0.96 \cdot 0.96 \cdot 0.96 \cdot 0.87) \cdot 100 = 38\%$$

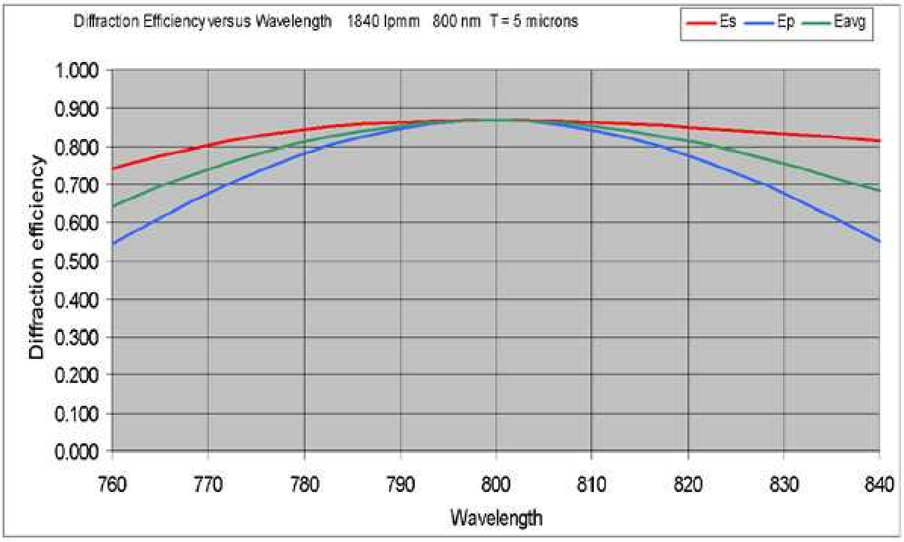

Figure 26: Diffraction efficiency vs. wavelength of the used gratings [32]

Position	Power / mW	Power / %	Loss / %
input	1.2	100	
after first (left) grating	0.95	79.2	20.8
at Fourier plane	0.8	66.7	15.8
after right cylinder mirror	0.69	57.5	13.8
output / after the second grating	0.55	45.8	20.3

Table 5: Transmitted power and losses of the mirrors and gratings

SLM Calibration

To drive the pulse shaper without a feedback loop it is necessary to characterize the properties of the LC-SLM. First the relation between applied voltage and the introduced phase and second the relation between the pixels and the effected wavelength has to be calibrated. With these two informations the laser pulse can be changed with the pulse shaper in a defined way.

Phase vs. Voltage Calibration

The used LC-SLM is a phase-only modulator. To calibrate the phase vs. voltage the LC-SLM is used outside the pulse shaper. The plane of polarization of the input light has to be 45° to the standard used horizontal polarization. This means that there is light polarized along the horizontal and the vertical axis and therefore parallel to the extraordinary and the ordinary axis of the liquid crystals. Applying voltage to the liquid crystals results in a change of the refraction index along the extraordinary axis and therefore a phase shift between the horizontally and vertically polarized light. If the phase shift between the two parts equals π the plane of polarization will be turned 90°. If there is a polarizer behind the LC-SLM aligned parallel to the incident light the setup works like an amplitude modulator where the transmitted light intensity depends on the applied voltage. In Figure 27 the dependence of the transmitted light intensity vs. applied voltage is shown. The maximum intensities are measured when the phase shift between ordinary and extraordinary beam is a multiple of 2π and the minimum intensities at odd multiples of π. As the refraction index is wavelength dependent a continuous monochromatic wave laser has to be used which a very small frequency spectrum has compared to a pulsed laser. If a HeNe is used there is a calibration curve to convert the data to the desired wavelength (in this case 800 nm). For the measurement data shown in Figure 27 the Ti:sapphire laser was used in continuous wave mode.

The transmission T dependent on the introduced phase ϕ between ordinary and extraordinary beam can be described as [33]

$$T = \cos^2\left(\frac{\phi}{2}\right) = \frac{1}{2}\cdot\left(1+\cos(\phi)\right) \tag{23}$$

where the phase can be rewritten as

$$\phi = 2\pi k + \arccos\left(2T - 1\right) \tag{24}$$

The term $2\pi k$ is necessary because it is not possible to calculate a phase greater than π with the arccos-function but the real phase shift is greater. The display manufacturer states that at maximum voltage the introduced phase is less than π [33] and therefore the minimum at a voltage of 1700 counts equals a phase shift of π. So the complete dependence of the introduced phase vs. applied voltage can be calculated (see Figure 28).

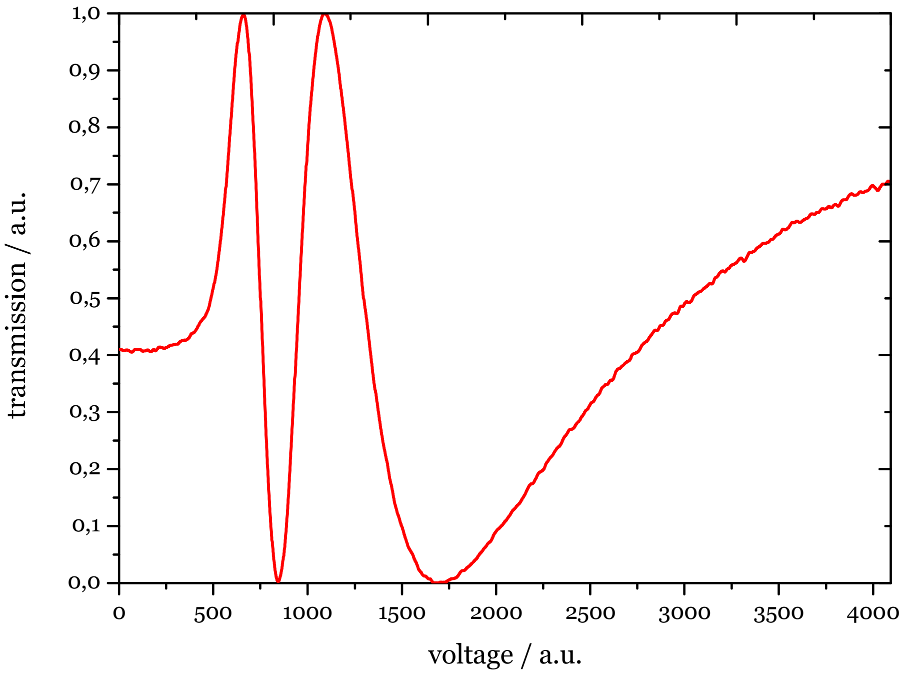

Figure 27: Transmitted light of the LC-SLM vs. applied voltage

Wavelength vs. Pixel Calibration

This calibration is necessary to know which wavelength is affected when a defined voltage / phase is applied to a pixel. To do this the LC-SLM is settled into the complete aligned pulse shaper and the Ti:sapphire laser is used in pulsed mode. If the LC-SLM had the ability for amplitude modulation all pixel would be set to zero transmission and one pixel to full transmission. Then the spectrum of the transmitted light is measured and the wavelength with peak intensity corresponds to the pixel which is set to full transmission. But the used LC-SLM is a phase-only modulator and so the same approach as above is used. The plane of polarization is turned to 45° and a polarizer is set behind the pulse shaper which yields an amplitude modulation. So one pixel after the other is set to full transmission at one time and the peak of the transmitted spectrum is recorded. The results are shown in Figure 29. Because the used fs-laser beam does not show a spectral width of about 90 nm the data are fitted and extrapolated.

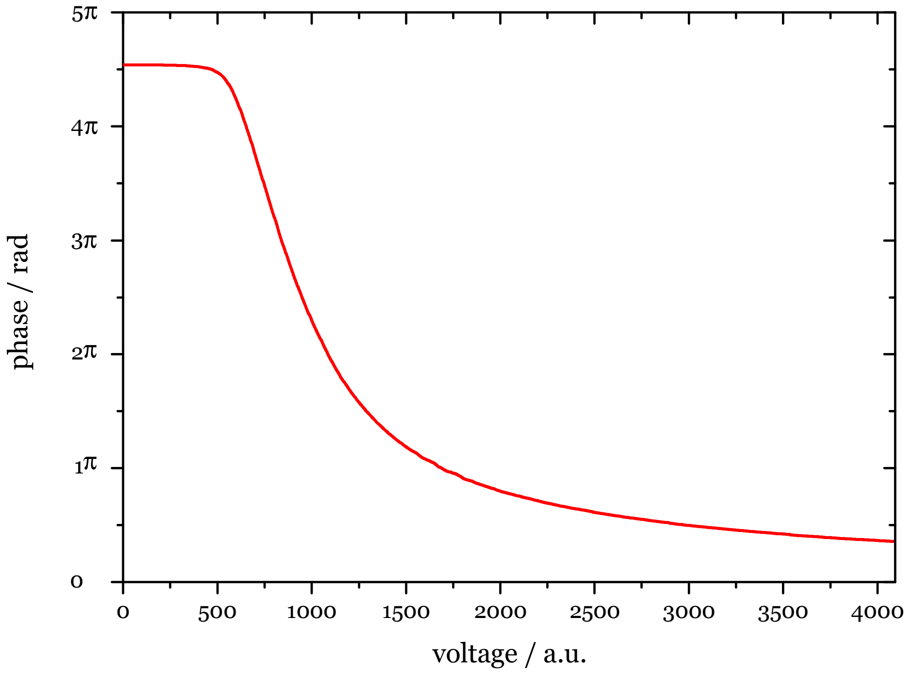

Figure 28: Introduced phase vs. voltage calibration

With this calibration data the pulse shape of the laser pulses can be changed in a defined way. But as the main setup has some unknown dispersions until now it was not spent much time on creating phase masks. In Figure 30 the autocorrelation of a double pulse shaped with the pulse shaper is shown. The shown shape at time delay zero is only due to the convolution of the autocorrelation. Only the outer two pulses exist. For generation of the double pulses it is necessary to set the pixels alternately to phase zero and phase π. If two or more consecutive pixels are set to zero phase and the same number of pixels to phase π the time delay between the double pulses is decreased which can be seen in Figure 30. Practically the sharp jumps between the pixels cannot be set due to the design of the liquid crystals and therefore the desired pattern will be smoothed. The effect is seen in the figure as the replicas of the centre pulse have a slightly different shape.

Similar to these experiments different sets of phases can be applied in order to control experiments by temporally shaped pulses.

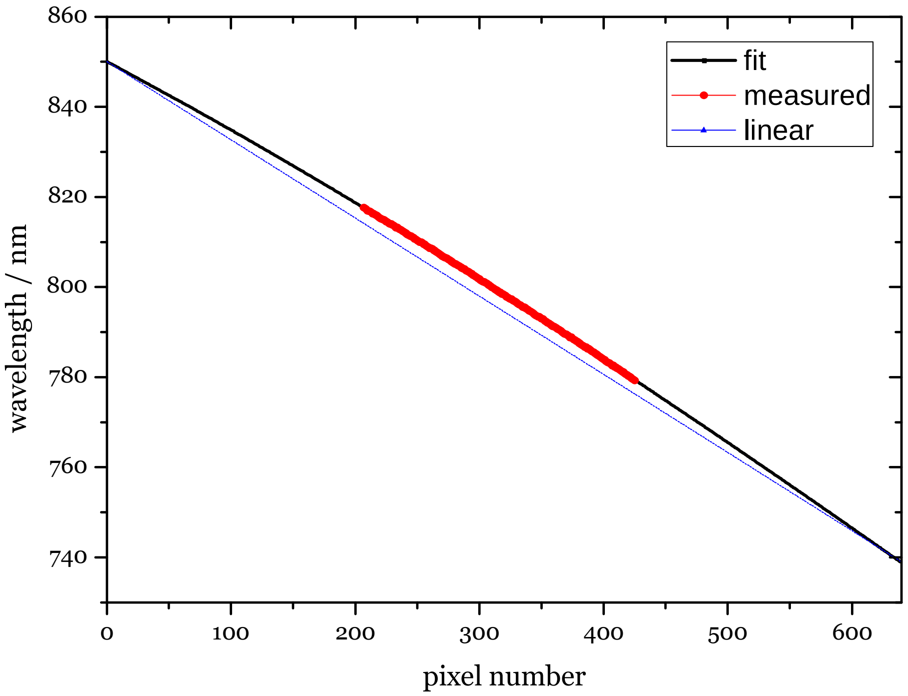

Figure 29: Wavelength vs. pixel number calibration

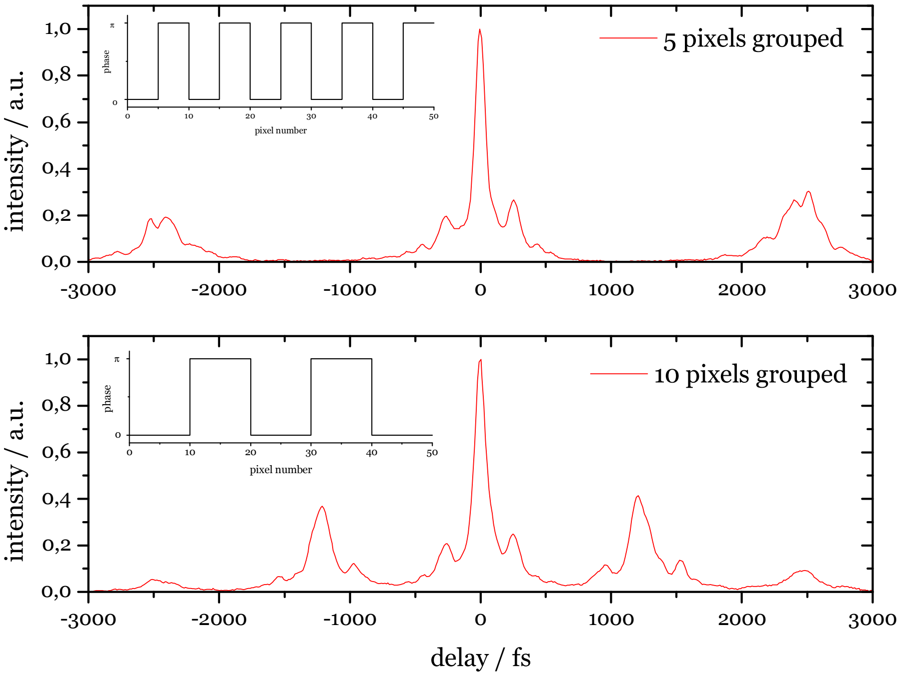

Figure 30: Autocorrelation trace of a double pulse shaped with the pulse shaper

4.4 Thin Film Ablation Experiments

It has been shown that the ablation threshold fluence F_{th} of thin thermally conducting films on thermally poor conducting substrates is lowered for nanosecond laser pulses when the film thickness d becomes less than the heat diffusion length L_{th}.

The heat diffusion length is defined by [34]

$$L_{th} = \sqrt{2D\tau} \tag{25}$$

where D is the thermal diffusivity and τ the pulse length. Due to the short pulse length of 60 fs, the longer electron-phonon relaxation time $\tau_{e\text{-}p}$ has to be considered and the pulse length τ should be replaced by $\tau_{e\text{-}p}$ [2, 3] in the formula above. $\tau_{e\text{-}p}$ for ta-C, in contrast to metals like gold [35] ($\tau_{e\text{-}p}$ ~710-830 fs [36]) , is comparatively low, i.e. ~220 fs [37].

In the following experiments DLC films were investigated using different pulse energies and numbers. Figure 31 shows typical cross sections of the ablated and modified surface recorded with the atomic force microscope. At high energies/fluences and a high number of pulses deep ablation craters are observed (a) whereas at single shot experiments and low fluences only a modification of the surface results (d). To yield the threshold fluences F_{th} the focal beam radius is determined with the D^2 vs. ln$E$ method [3]

$$D^2 = 2w_0^2 \ln\frac{E}{E_{th}} = 2w_0^2\left(\ln E - \ln E_{th}\right) \tag{26}$$

where D^2 is the squared diameter of the crater, w_0 the beam radius, E the pulse energy, and E_{th} the threshold pulse energy. With the knowledge of the focal beam diameter the dependence of the squared crater diameter according to the logarithmic fluence can be shown (Figure 32) and the threshold fluence F_{th} calculated.

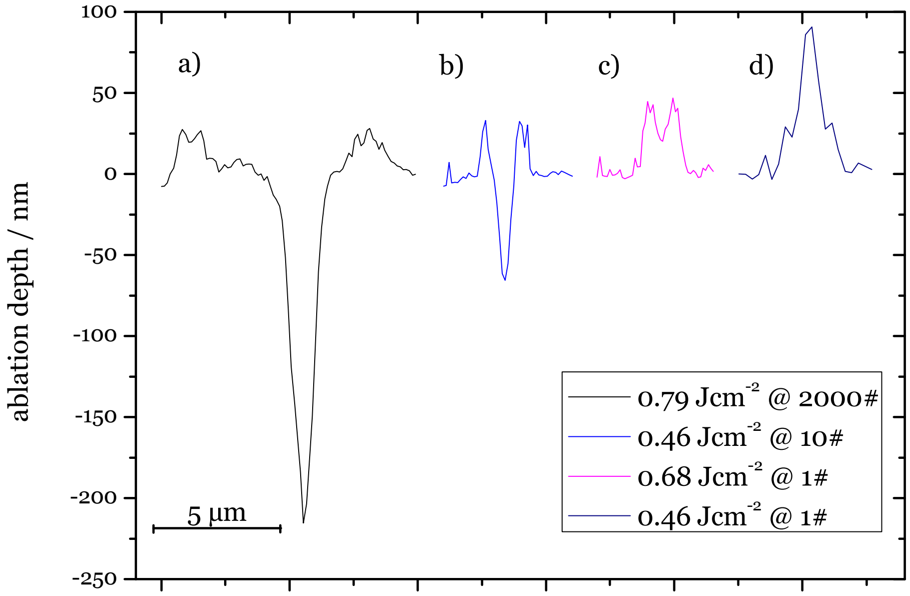

Figure 31: AFM topographies show typical ablated and modified surfaces

It can be seen that the higher the number of pulses the lower is the threshold fluence. This relation is described by the incubation factor ξ [38]

$$F_{th}(N) = F_{th}(1) \cdot N^{\xi-1} \tag{27}$$

where $F_{th}(N)$ is the ablation threshold fluence for N laser pulses, $F_{th}(1)$ is the threshold for one laser pulse, and ξ is the material-dependent incubation factor. In Figure 33 the dependence of $F_{th}(N)*N$ vs. N on a double logarithmic is shown.

$$\log(F_{th}(N) \cdot N) = \xi \log(N) + \log(F_{th}(1)) \tag{28}$$

The data are linearly fitted and extrapolated to N=1 which yields $F_{th}(1)$=0.39 Jcm^{-2}. The slope corresponds to an incubation factor ξ=0.86 agreeing with that of the substrate material silicon determined with 30 fs pulses [39].

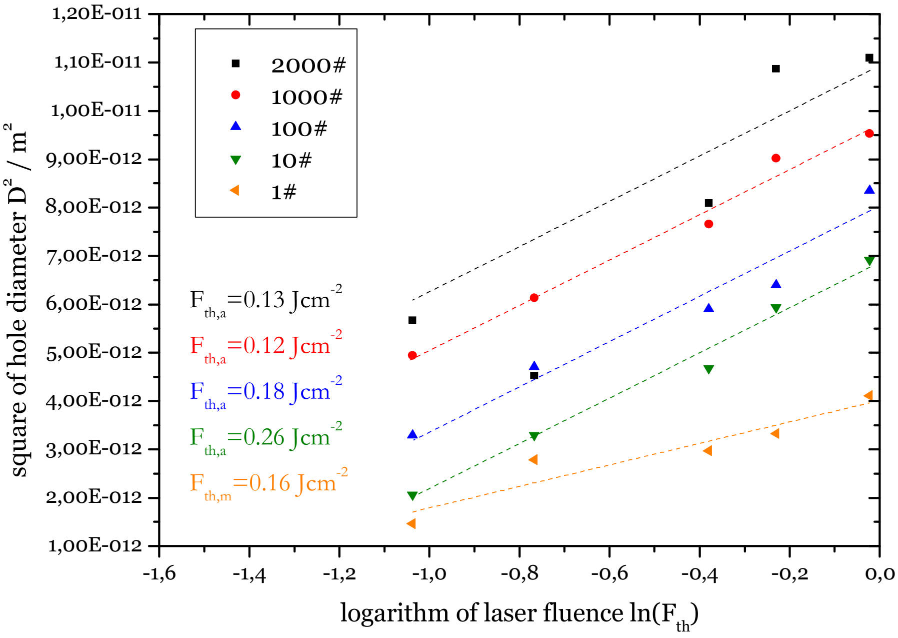

Figure 32: Determination of threshold fluence for modification (one shot) and ablation

In Figure 34, the dependence of the single pulse modification threshold fluence $F_{th}(1)$ depending on the film thickness is shown. $F_{th}(1)$ is lowered below a film thickness d of 60 nm. In this thickness region, $F_{th}(1)$ increases linearly with d in accordance with our new model where all energy is dissipated in the volume of the film described by d and the beam diameter. The thickness d, where $F_{th}(1)$ starts becoming independent of d, corresponds to

$$d = L_{th} + \alpha^{-1} \tag{29}$$

where L_{th} is the thermal diffusion length and α^{-1} the optical absorption length. Since $L_{th} << \alpha^{-1}$, the thermal diffusion is negligible in this case, and the optical absorption length

α^{-1} controls the energy density. This contrasts to gold films, where the electronic diffusivity is mainly determining the ablation threshold, since the electron-phonon coupling is much weaker in gold and α^{-1} = 12 nm [35].

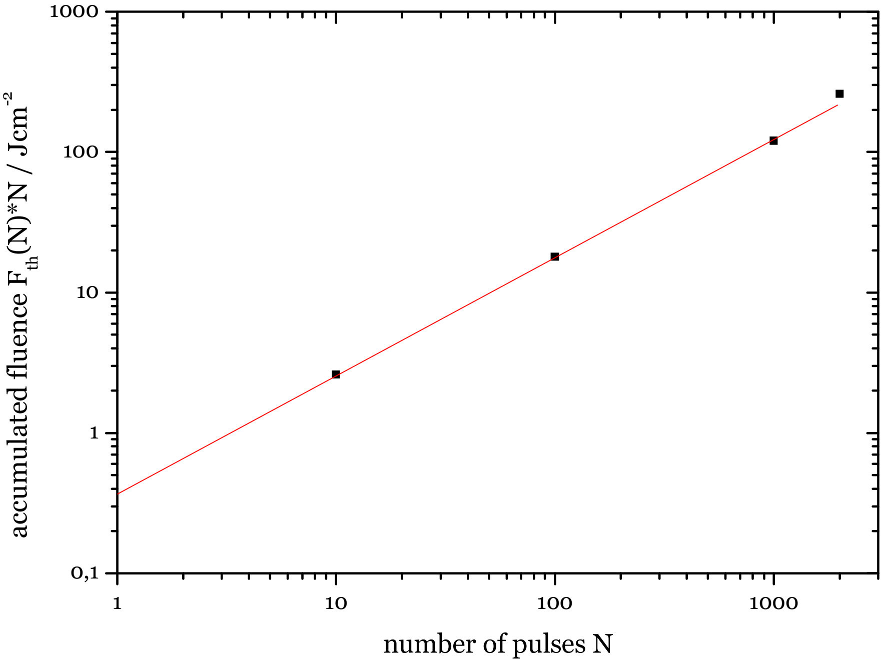

Figure 33: Incubation factor for silicon ablation equals ξ=0.86

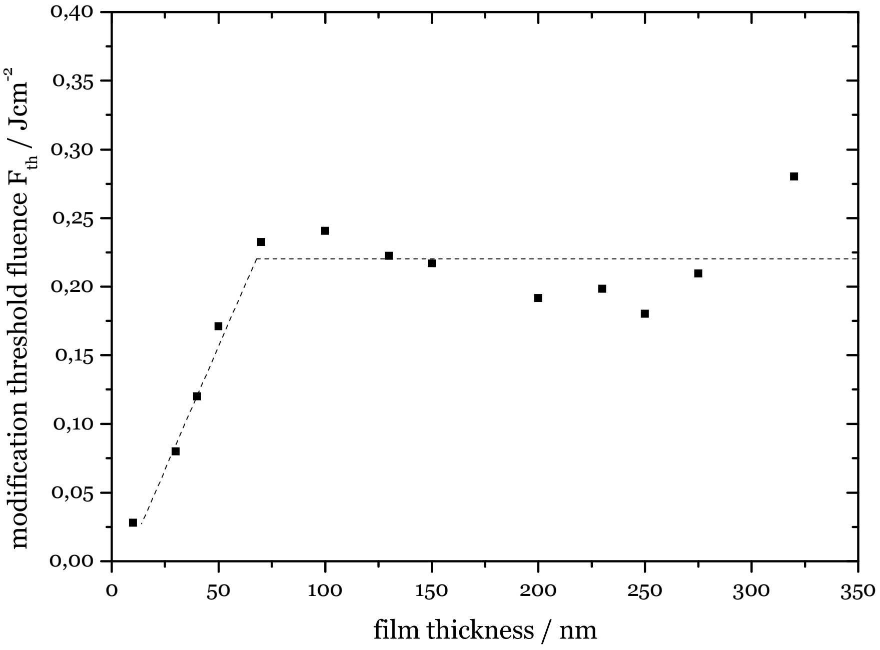

Figure 34: Single pulse modification thresholds depending on film thickness

These results show that the modification thresholds determined for bulk materials cannot be compared to thin film modification thresholds. Various surface effects have to be considered in order to predict modification fluences.

5 Conclusion and Outlook

It has been shown that the current laser setup is a very flexible and powerful tool to carry out many kinds of experiments. Especially the usage of the pulse shaper leads to promising results. Up to now only fixed masks were applied to the LC-SLM resulting in static laser pulse shapes. Because the input pulse and the LC-SLM have to be characterized well the experimental effort is quite high. Using a static approach it can be very exhausting to gain an optimal output pulse shape for a defined task. As the LC-SLM is controlled by the computer it is possible to drive the pulse shaper setup in a feedback controlled loop. Therefore a feedback parameter from the experiment has to be fed to the computer which adaptively optimizes the applied mask to optimize the experiment. Currently the pulse shaper is tested with the feedback control loop to minimize the pulse length by maximizing the SHG signal. Comparing the LC-SLM display in use to former SLM types (128 pixels) the higher number of pixels (640 pixels) enables us to gain better temporal resolution. Furthermore, the electronics for LC displays is getting faster and therefore allows multiple changes of the phase mask per second.

Single shot experiments reveal a modification of thin DLC films with volume increase followed by the ablation of the completely converted low density phase in analogy to the ablation of carbohydrate polymers. This demonstrates that multi-fs-pulse processes are concerned with highly incubated carbonaceous materials. The modification threshold of nanoscale DLC films with single pulse treatments, is lowered below a film thickness of 60 nm. Due to strong electron-phonon coupling the optical absorption length controls the behaviour of the modification threshold in contrast to gold films, where the electronic diffusivity is mainly determining the modification threshold, since the electron-phonon coupling is much weaker. These results demonstrate that dynamic properties of nanoscale materials can be directly investigated by fs-laser modification evaluations.

6 Appendix

The program for acquiring the autocorrelation trace is written in LabVIEW. The front panel is shown in Figure 35. At the top right the frequency spectrum is shown as it is very important for optimizing the laser pulses. A previously stored “good working” frequency spectrum can be loaded to compare it with the actual one. If the actual one is too different from the stored one the laser pulses will not be appropriate.

At the bottom left the control panel can be found where the approximate number of acquisition data and the acquisition frequency can be set. Further the position of the stage, where the two split pulses overlap perfectly, can be set as well as the size of the delay scan window. Care has to be taken because it is not possible to set maximum acquisition frequency at maximum data points and maximum scan area. The position of maximum intensity only needs to be set roughly. There is a button on the right side called “Auto x-Offset” for the fine adjustment to set the autocorrelation peak to the centre of the scan area. At zero intensity the measured voltage of the photodiode is not zero but it can be set to zero in the program with the button “Auto y-Offset”.

After starting the data acquisition the autocorrelation data are displayed at the bottom right. Next to this window some values are shown which correspond to the measured pulse length. The peak FWHM corresponds to the fitted Gaussian shape which analyses only the intensities greater than 40 % of the maximum intensity. If there are side wings they will not affect this value. As the real pulse length is a factor 1.41 shorter than the FWHM of the autocorrelation trace, the value will be displayed in “peak pulse length”. Underneath these two values there are the corresponding values but including the whole intensity dataset. For a good laser pulse setting the values of the peak and the whole dataset should be the same which reveals no side wings. The delay between the overlapping pulses is generated by the movement of a translational stage which is shown in the window on the top right.

It is possible to store a single autocorrelation trace and its corresponding frequency spectrum to a data file by marking the check box “Single Shot & Save” for later use.

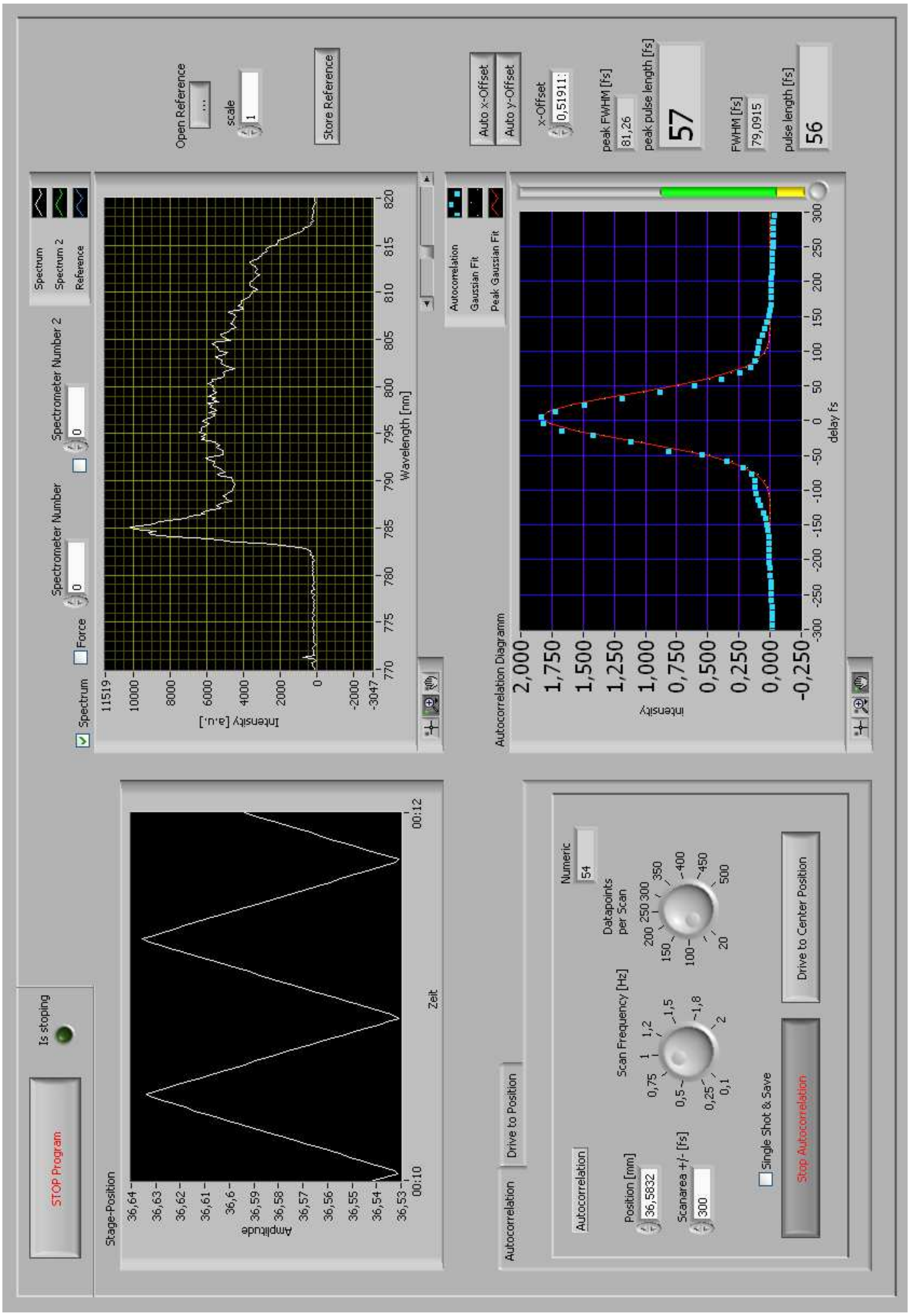

Spectrometer Number 0

Spectrometer Number 2 0

scale 1

x-Offset 0,51911

peak FWHM [fs] 81,26

peak pulse length [fs] 57

FWHM [fs] 79,0915

pulse length [fs] 56

Position [mm] 36,5832

Scanarea +/- [fs] 300

Numeric 54

☐ Single Shot & Save

Figure 35: Front panel of the program measuring the autocorrelation

Bibliography

[1] T. H. Maiman, *Stimulated Optical Radiation in Ruby*, *Nature* **1960**, *187*, 493.

[2] J. Krüger, W. Kautek, *The femtosecond pulse laser: a new tool for micromachining*, *Laser Physics* **1999**, *9*, 30.

[3] J. Krüger, W. Kautek, *Ultrashort pulse laser interaction with dielectrics and polymers*, *Polymers and Light* **2004**, *168*, 247.

[4] Y. X. Yan, E. B. Gamble, K. A. Nelson, *Impulsive Stimulated Scattering - General Importance in Femtosecond Laser-Pulse Interactions with Matter, and Spectroscopic Applications*, *Journal of Chemical Physics* **1985**, *83*, 5391.

[5] L. Dhar, J. A. Rogers, K. A. Nelson, *Time-Resolved Vibrational Spectroscopy in the Impulsive Limit*, *Chemical Reviews* **1994**, *94*, 157.

[6] A. Rundquist, J. Broman, D. Underwood, D. Blank, *Polarization-dependent detection of impulsive stimulated Raman scattering in alpha-quartz*, *Journal of Modern Optics* **2005**, *52*, 2501.

[7] R. Trebino, *Frequency-resolved optical gating: the measurement of ultrashort laser pulses*, Kluwer Academic Publishers, **2000**.

[8] D. Meschede, *Optik, Licht und Laser*, 2nd ed., Teubner Verlag, **2005**.

[9] C. Rullière, *Femtosecond laser pulses : principles and experiments*, 2nd ed., Springer, **2005**.

[10] P. Rüdiger, *Encyclopedia of Laser Physics and Technology*, http://www.rp-photonics.com/encyclopedia.html last accessed 26.4.2009

[11] U. Keller, *Recent developments in compact ultrafast lasers*, *Nature* **2003**, *424*, 831.

[12] W. T. Silfvast, *Laser fundamentals*, 2nd ed., Cambridge University Press, **2004**.

[13] F. Krausz, T. Metzger, J. Rauschenberger, A. Apolonski, K. Schmid, A. Baltuska, *Ultrakurze Laserpulse: Erzeugung und Anwendung*, *Laser Technik Journal* **2005**, *2*, 27.

[14] G. Steinmeyer, *Wie misst man kurze Laserpulse? Welche Verfahren gibt es?*, *Laser Technik Journal* **2005**, *2*, 34.

[15] S. Naumov, A. Fernandez, R. Graf, P. Dombi, F. Krausz, A. Apolonski, *Approaching the microjoule frontier with femtosecond laser oscillators*, *New Journal of Physics* **2005**, *7*.

[16] E. B. Treacy, *Optical Pulse Compression with Diffraction Gratings*, *Ieee Journal of Quantum Electronics* **1969**, *Qe 5*, 454.

[17] R. L. Fork, O. E. Martinez, J. P. Gordon, *Negative Dispersion Using Pairs of Prisms*, *Optics Letters* **1984**, *9*, 150.

[18] I. A. Walmsley, V. Wong, *Characterization of the electric field of ultrashort optical pulses*, *Journal of the Optical Society of America B-Optical Physics* **1996**, *13*, 2453.

[19] C. Iaconis, I. A. Walmsley, *Spectral phase interferometry for direct electric-field reconstruction of ultrashort optical pulses*, *Optics Letters* **1998**, *23*, 792.

[20] A. M. Weiner, *Femtosecond pulse shaping using spatial light modulators*, *Review of Scientific Instruments* **2000**, *71*, 1929.

[21] D. Yelin, D. Meshulach, Y. Silberberg, *Adaptive femtosecond pulse compression*, *Optics Letters* **1997**, *22*, 1793.

[22] A. Assion, T. Baumert, M. Bergt, T. Brixner, B. Kiefer, V. Seyfried, M. Strehle, G. Gerber, *Control of chemical reactions by feedback-optimized phase-shaped femtosecond laser pulses*, *Science* **1998**, *282*, 919.

[23] P. R. Willmott, J. R. Huber, *Pulsed laser vaporization and deposition*, *Reviews of Modern Physics* **2000**, *72*, 315.

[24] L. Egerhazi, Z. Geretovszky, T. Szorenyi, *Thickness distribution of carbon nitride films grown by inverse-pulsed laser deposition*, *Applied Surface Science* **2005**, *247*, 182.

[25] L. Egerhazi, Z. Geretovszky, T. Szorenyi, *Inverse pulsed laser deposition*, *Applied Physics a-Materials Science & Processing* **2008**, *93*, 789.

[26] A. Sennaroglu, J. G. Fujimoto, *Design criteria for Herriott-type multi-pass cavities for ultrashort pulse lasers*, *Optics Express* **2003**, *11*, 1106.

[27] Femtosoft Technologies, *Frog 3.2.2*, http://www.femtosoft.biz/demo.shtml last accessed 26.4.2009

[28] J. Robertson, *Diamond-like amorphous carbon*, *Materials Science & Engineering R-Reports* **2002**, *37*, 129.

[29] Z. Geretovszky, T. Szorenyi, *Compositional and thickness distribution of carbon nitride films grown by PLD in the target plane*, *Thin Solid Films* **2004**, *453-54*, 172.

[30] J. Köhler, Kompakter, flexibler und hochauflösender 2x640 Pixel-Pulsformer für Femtosekunden-Laserpulse; Technische Dokumentation, **2003**.

[31] TOPAG, *Laser Optik Katalog*, http://www.topag.de/komponenten/optik.html last accessed 25. 4. 2009

[32] Wasatch Photonics, *Efficiency of Transmission Gratings*, http://www.wasatchphotonics.com/gratingspecs/Dickson1840lpmmVolumePhaseHolographicTransmissionGratingfor800nm.htm last accessed 25. 4. 2009

[33] CRI, Spatial Light Modulator Systems User Manual, 1.3 ed., Cambridge Research & Instrumentation, Inc., **2004**.

[34] E. Matthias, J. Siegel, S. Petzoldt, M. Reichling, H. Skurk, O. Kading, E. Neske, *In-Situ Investigation of Laser-Ablation of Thin-Films*, *Thin Solid Films* **1995**, *254*, 139.

[35] J. Krüger, D. Dufft, R. Koter, A. Hertwig, *Femtosecond laser-induced damage of gold films*, *Applied Surface Science* **2007**, *253*, 7815.

[36] R. H. M. Groeneveld, R. Sprik, A. Lagendijk, *Femtosecond Spectroscopy of Electron-Electron and Electron-Phonon Energy Relaxation in Ag and Au*, *Physical Review B* **1995**, *51*, 11433.

[37] E. Carpene, E. Mancini, C. Dallera, D. Schwen, C. Ronning, S. De Silvestri, *Ultrafast carrier dynamics in tetrahedral amorphous carbon: carrier trapping versus electron-hole recombination*, *New Journal of Physics* **2007**, *9*.

[38] Y. Jee, M. F. Becker, R. M. Walser, *Laser-Induced Damage on Single-Crystal Metal-Surfaces*, *Journal of the Optical Society of America B-Optical Physics* **1988**, *5*, 648.

[39] J. Bonse, S. Baudach, J. Kruger, W. Kautek, M. Lenzner, *Femtosecond laser ablation of silicon-modification thresholds and morphology*, *Applied Physics a-Materials Science & Processing* **2002**, *74*, 19.

Abbreviations

AFM	atomic force microscope
BBO	β-barium borate
cw-laser	continuous wave laser
DLC	diamond-like carbon
FROG	frequency-resolved optical gating
fs	femtosecond = 10^{-15} seconds
FWHM	full width at half maximum
HeNe-laser	helium neon laser
IPLD	inverse-pulsed laser deposition
KD*P	potassium dideuterium phosphate
KrF-laser	krypton fluoride laser
LC SLM	liquid crystal spatial light modulator
NA	numerical aperture
Nd:YAG	neodymium doped yttrium aluminium granet
Nd:YVO_4	neodymium doped yttrium vanadate
nm	nanometer = 10^{-9} meter
PLD	pulsed laser deposition
ps	picosecond = 10^{-12} seconds
$sech^2$	squared hyperbolic secant function
SHG	second harmonic generation
SLM	spatial light modulator
SPIDER	spectral interferometry for direct electric-field reconstruction
UV	ultra violet

List of Figures

List of Tables

Abstract

A main focus of this diploma work was the characterization of femtosecond laser pulses. A LabVIEW program for autocorrelation measurements was adapted to deliver results at an interval of up to 2 Hz and a FROG (frequency-resolved optical gating) device was developed to characterize the phase of laser pulses. Ablation experiments were carried out to determine the dependence of the fs-laser ablation threshold on the thickness of thin diamond like films. These experiments served as preparation for the setup, adjustment, and calibration of a pulse shaper in a new configuration with a high-power femtosecond oscillator.

Kurzfassung

Ein wichtiger Bestandteil dieser Diplomarbeit war die Charakterisierung von Femtosekunden-Laserpulsen. Dazu wurde das bestehende LabVIEW Programm für die Autokorrelationsmessungen adaptiert und ermöglicht nun Messungen mit einer Geschwindigkeit von bis zu 2 Hz. Ebenfalls wurde ein FROG (frequency-resolved optical gating) aufgebaut, womit auch die Phasenanteile der Femtosekunden-Laserpulse gemessen werden können. Mittels Ablationsexperimenten wurde die Abhängigkeit der Ablationsschwelle von der Filmdicke von diamantähnlichen Kohlenstoffschichten ermittelt. Zur erweiterten Durchführung von Ablationsexperimenten wurden der Aufbau, die Justage und die Kalibrierung eines Pulsformers in Kopplung eines leistungsstarken Femtosekundenoszillators realisiert.

Curriculum Vitae

Personal Details

Name	Christian Haselberger
Date of Birth	18. März 1982
Nationality	Austria

Education

2004 - 2009	University of Vienna Study Program Chemistry Diploma Theses “Laser Beam Engineering for Material Processing”
2002 - 2005	University of Applied Sciences Technikum Wien Study Program Electronics Diploma Theses “ Prototyp für Blob-basiertes Tracking mehrerer Personen in Videodaten“
1996 - 2001	HTL for Electronics / Automation Karlstein / Thaya
1992 - 1996	Secondary Modern School Waldhausen / Strudengau
1988 - 1992	Elementary School Dorfstetten